Concerted elimination of Cl_2^+ from CCl_4 and of I_2^+ from CH_2I_2 driven by intense ultrafast laser pulses

A Thesis Presented

by

Dominik Peter Michael Geissler

to

The Graduate School

in Partial Fulfillment of the Requirements

for the Degree of

Master of Arts

in

Physics

Stony Brook University

December 2007

Stony Brook University

The Graduate School

Dominik Peter Michael Geissler

We, the Thesis committee for the above candidate for the Master of Arts degree, hereby recommend acceptance of the Thesis.

Thomas C. Weinacht, Thesis Advisor

Assistant Professor, Department of Physics and Astronomy

Dominik A. Schneble

Assistant Professor, Department of Physics and Astronomy

Michael A. Zingale

Assistant Professor, Department of Physics and Astronomy

This Thesis is accepted by the Graduate School.

Lawrence Martin

Dean of the Graduate School

Abstract of the Thesis

Concerted elimination of Cl_2^+ from CCl_4 and of I_2^+ from CH_2I_2 driven by intense ultrafast laser pulses

by

Dominik Peter Michael Geissler

Master of Arts

in

Physics

Stony Brook University

2007

The concerted elimination of Cl_2^+ from CCl_4 and I_2^+ from CH_2I_2 is studied with various methods. Single pulse experiments proved the possibility of Cl_2^+ elimination from CCl_4 but were limited by background contamination. Pulse shape varying experiments (with use of a genetic algorithm) demonstrated a pulse shape dependent concerted elimination of I_2^+ from CH_2I_2. Furthermore it was possible to partly resolve the involved molecular states for this elimination process by pump probe scans both in the red as in the UV spectrum. We could follow the evolution of a vibrational wave packet in the halogenated methane

CH_2I_2 and observed how the wave packet modulates both dissociation and concerted elimination to form CH_2I^+ and I_2^+ respectively. Finally a simple and intuitive interpretation of the molecular dynamics leading to the formation of the products is presented.

To Martin and my family

Contents

List of Figures

Acknowledgements

First, I would like to thank my advisor Tom Weinacht for giving me the opportunity to work with him. He supported my work in many different ways: He introduced me to the lab, there have been lot of fruitful discussions and he spread an enthusiasm that made all the long hours and disappointments look minuscule. I also want to thank Sarah Nichols and Brett Pearson for their sher infinite patience to answer my questions and helping me out with my experiment many times. Also all other members of the group Carlos, Stephen, Coco and Marija have to be mentioned here, as I enjoyed working together with them very much.

Furthermore I want to thank everyone with whom I spent great times outside the lab and who made my stay an integrated experience.

I owe a debt of gratitude to everyone who was involved in the exchange program between the physics departments of the University of Wrzburg and Stony Brook University for all their effort to organize my stay here. A scholarship

from the German Merit Foundation (Studienstiftung des deutschen Volkes) provided the financial framework and is highly appreciated, too. In addition, this work was supported by the National Science Foundation.

My warmest thanks go to my family for always encouraging me. Without their support I would not have been able to come here and begin this work, nor finish it. Last but not least, I would like to thank my boyfriend Martin for his love and encouragement.

Chapter 1

Introduction

The idea of generating short laser pulses to observe short processes in nature came up soon after the invention of the laser. Since then vast progress has been made in shortening the pulse duration and increasing the pulse power. Pulse durations in the sub-femtosecond time scale have been reported [11]. Current (2005) records in energy are high power 10 fs pulses at 10.5 mJ [41]. In the meantime ultrafast laser systems are available for a continuous spectrum from near IR to UVC for their central wavelength. They have broad application to observe processes that happen on a femtosecond timescale, like atomic/molecular transitions or reactions and solid-state phenomena. At the same time their high intensity surpasses the characteristic fields in atoms or molecules, i.e. $E > \frac{e}{4\pi\epsilon_0 r_{\mathrm{Bohr}}}$. The progress in laser technology has been accompanied by the development of techniques for pulse shaping, allowing control

over the characteristic variables of the electric field: phase, amplitude, and polarization. This opened the field of ultrafast control to interact with atomic and molecular processes. Progress has been made in controlling selective atomic and molecular excitation and selective molecular fragmentation [4, 9, 14, 40].

Femtosecond lasers are ideal to study vibrational wave packet dynamics. They can be used for molecular imaging and play an important role in driving coherent chemistry [1, 18, 35, 37, 42]. Several diatomic molecules have been studied so far, such that research is proceeding to larger molecules. Halogenated methanes make up a broad field of interesting candidates. With them several experiments ([31], [43] and [22]) have been done in examining the control over concerted elimination and bond breaking.

In this thesis some experiments will be described and discussed which examine the concerted elimination of molecular halogens from halogenated methanes under femtosecond laser excitation. The model systems CH_2I_2 and CCl_4 have been studied, i.e. reactions like:

$$CCl_4 + nh\nu \rightarrow Cl_2^+ + \ldots$$

$$CH_2I_2 + nh\nu \rightarrow I_2^+ + \ldots$$

There are principally two ways to emit molecular particles from the parent molecule: (a) both halogen atoms are emitted separately and combine afterwards, if their pathes cross or (b) both halogen atoms are emitted and

combine at the same time. Latter process is referred to *concerted* elimination (this definition follows [23]) and is directly dependent on the vibrational and rotational motion of the molecule.

The aim of this thesis is to develop a simple picture of the involved molecular transitions for the concerted formation of the halogen molecules and to study the controllability of this process. Therefore different approaches have been used: Single pulse experiments ("genetic algorithm experiments") in combination with a pulse shaper payed attention to the influence of different pulse shapes, double pulse ("pump-probe") experiments examined the time dynamics of this process and experiments with mixed UV and IR laser searched for an influence of the laser wavelength.

Chapter 2

The experimental apparatus

2.1 The laser system

In the experiments a high power Ti:Sapphire laser system is used, as it is described in [3]. It consists of a Ti:Saphire oscillator, that emits 30 fs laser pulses with a wavelength of about 780 nm at a repetition rate of 85 kHz and an energy of about 6 nJ. The oscillator is pumped by a commercial VERDI laser (with 532 nm wavelength). These pulses are used as a seed for the Ti:Sapphire amplifier (pumped by a commercial Quantronix laser at 532 nm). Finally the amplifier generates pulses with a time duration of about 30 fs with a repetition rate of 1 kHz. The pulse energy reaches up to 1 mJ. The spectrum can be described best as a sum of two gaussian curves, in which the main Gaussian distribution around 780 nm usually has a bandwidth of about 30 nm.

For this project basically two different setups are used. The first one has been built by several members of the group before and uses one ("GA experiments") or two red pulses ("red/red pump-probe experiments") that interact with a cloud of molecules inside a vacuum chamber. This setup is roughly described in the following paragraphs. The second one involves double pulse experiments with a red and a UV pulse ("UV/red pump-probe experiments") instead. This new setup is described in more detail in section 2.6.

For some of the experiments the laser pulse is modified in our pulse shaper (for a schematic view see 2.1). Here the phase (in frequency domain) of the pulses is modified, as well as their overall intensity. At the heart of the pulse shaper are two gratings and the accusto-optical-modulator (AOM crystal). The first grating splits up the beam into its different frequencies, i.e. it maps different frequencies to different propagating angles. Then this bundle is reflected by a curved mirror and focussed inside the AOM crystal, so that now the different angles (and herewith frequencies) are mapped to different points inside the AOM. A piezzo crystal is attached to the side of the AOM. It can be modulated by a radio frequency signal (around a carrier frequency of 150 MHz) generated by one of our lab computers. Thereby it launches a sound wave inside the AOM and thus writes a diffraction pattern in the crystal. The phase of this pattern determines the final phase of the diffracted laser pulse. The

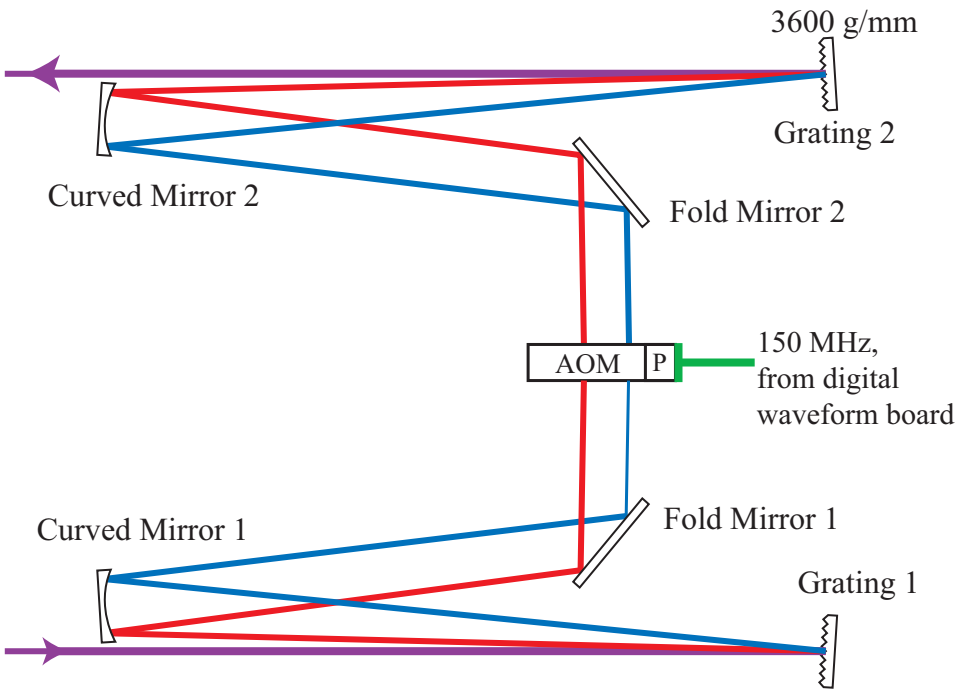

Figure 2.1 Schematic view of the pulse shaper: The piezzo crystal (P) is controlled by the radio signal. This excites sonic waves inside the accusto-optical-modulator (AOM).

amplitude of the sound wave influences the intensity of the diffracted light. This process is triggered by the pump laser and the RF signal and can be considered constant for the time of the laser pulse passing through the crystal. The second grating and curved mirror pair reverses the spectral mapping in space of the first one and recombines all frequencies (now with modified phases) to one beam. The pulse shaper has an overall efficiency of about 30% and can write a maximum phase difference of 60π across the whole bandwidth of the laser.

For some experiments two laser pulses are used. The setup resembles a Mach-Zehnder-Interferometer. After a beam splitter, these pulses follow different paths. One of them passes through the pulse shaper and thus can be modified. The other is sent to a delay stage. This stage is equipped by a motor, that can be controlled by the lab computer. The lab software has control over the position of the stage and thus the path length for the second beam line. Herewith the time difference in delay time of both pules at the chamber can be varied automatically. The minimal step size of the stage corresponds to a resolution of their time difference of 0.33 fs. Finally both beams are focussed inside the vacuum chamber by a lens. Usually for these experiments both pulses have an energy of about 200 μJ.

Figure 2.2 summarizes the experimental laser setup described so far.

2.2 The interaction chamber

All experiments are performed inside a vacuum chamber. Figure 2.3 shows a schematic view of the vacuum chamber. The interaction chamber itself is pumped by a turbo pump that establishes a vacuum pressure of about 10^{-6} Torr.

The molecules are injected from the sample manifold through a small nozzle. All substances discussed in this thesis have sufficient vapor pressure (at

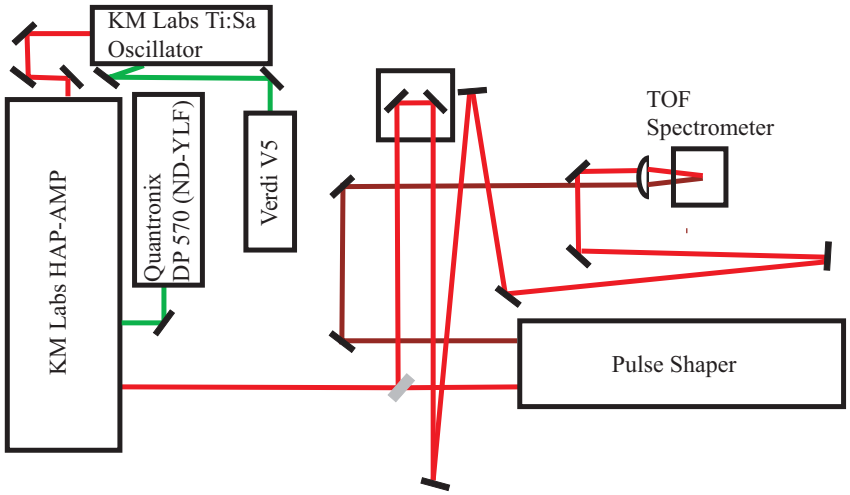

Figure 2.2 Schematic view of the red experimental setup: The green lines represent the 532 nm pump beam, the red line the used 780 nm beam line, and the dark red line the modified pulses by the amplifier. (figure from [20])

room temperature) to receive a sufficient signal. A small reservoir between the sample manifold and the chamber (with separate valves to open) makes sure that the pressure in the molecular beam is independent of the actual vapor pressure in the sample holder, but only depends on the number of molecules inside the reservoir. Furthermore the reservoir is big enough compared to the injection nozzle to guarantee a molecular beam with constant pressure. Only in long time experiments (> 1 hour) a linear pressure decay becomes noticeable. The final working pressure in the chamber with some sample molecules is usually around 10^{-5} Torr. The fact that a molecular beam is used has two convenient consequences: (a) Each laser pulse "sees" a new cloud of sample

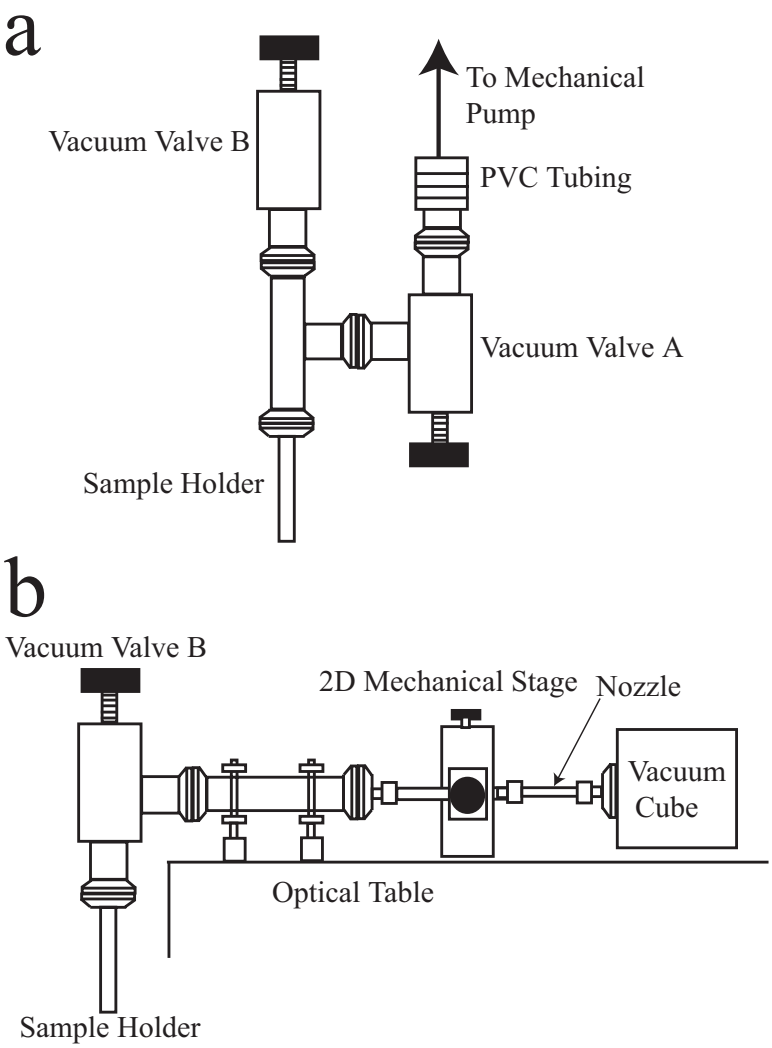

Figure 2.3 Schematic view of vacuum system. Top panel: Front view of manifold. Bottom panel: Side view. (figure from [25])

molecules, so that one does not have to worry about long time changes in the composition of fragments. (b) The average free propagation length of each molecule is much longer than the diameter of the molecular beam. This is especially important as it means that fragments and formed radicals due to laser excitation do not have time to react with other molecules, such that detected ions have to be derived from only one parent molecule.

The laser beam (or in pump-probe experiments, both beams) enters the chamber through a thin ($250\,\mu$m) sapphire window, so that the additional group velocity dispersion is negligible. Before that the beams are focused by a lens. It is adjusted such that the focal point is located within the molecular beam.

2.3 The red-red pump-probe alignment

The pump-probe experiments use both arms of the Mach-Zehnder interferometer. Pulses from both arms are focussed in an non-collinear setup inside the chamber. This means that inside the crossing volume the phase difference between both pulses is not well defined. In particular this explains the absence of observable interference fringes.

For each two pulse experiment, the system has to be aligned, such that spatial overlap of both pulses inside the chamber is established. For this pur-

pose a lens after the chamber maps the laser focal point inside the chamber to a white paper card. Here the optimal position for spatial overlap and maximal detector yield is marked, so that its is easy to reproduce the alignment.

In order to adjust temporal overlap of both pulses, a similar setup is used. The imaging lens after the chamber images the focal point inside the chamber into a frequency mixing crystal (BBO: $\beta - BaB_2O_4$) cut for second harmonic generation. This crystal emits blue light between both frequency doubled red beams, if and only if both pulses arrive in the chamber at the same time.

The intensity of the unshaped pulse is fixed for each run, but can be varied manually by opening and closing one iris in the beam path. As the second pulse comes from the pulse shaper, there is the possibility to change its intensity automatically via computer control.

After the unshaped pulse energy is adjusted manually with the irises and a common power meter, the computer can be set to vary the remaining parameters. The final result is a three dimensional data set, that saves the time-of-flight-mass-spectrum (4000 to 6000 sampling points) for each time difference between shaped and unshaped pulse (in a certain range and step size), and for each energy of the shaped pulse (from total to zero energy).

2.4 The detector and data acquisition

Our time-of-flight-mass-spectrometer (TOFMS) is configured to detect only positive ions. The detector sits above the interaction point. The cations are accelerated by a an applied voltage difference (750 V) and can escape through a small hole into the detection tube. Finally they reach microchannel plates that detect the single particles. The signal output is connected to a digital oscilloscope integrated in one of our lab computers. The oscilloscope is triggered with the laser pulse and can sample the signal with a rate of up to 500MHz. A typical trace is shown in figure 2.4. The y-axis shows the detector signal (in an arbitrary unit) for each sampling point numbered from 0 (trigger time) till the end of the trace.

So the sampling point corresponds to time difference between trigger time and detector signal and thus yields the flight time of a certain particle. Furthermore the accelerating field is roughly homogeneous and constant in time, so that this time is related to the particles' charge-to-mass ratio $\frac{q}{m}$. After a re-calibration of the x-axis from flight time to $\frac{q}{m}$, one can assign each peak to a certain ion. As the types of possible ions is limited by the sample molecule (and perhaps contaminations from former experiments) the assignment is mostly unique for the experiments performed in this thesis, besides few ambiguities like X_2^{++} or X^+. The length of the TOF tube is short enough, so that the

fragments of two succeeding pulses do not overlap.

Special care has to be taken for the pressure inside the chamber. Although higher pressure would give a stronger signal, it has disadvantages: A high ion flux shortens the lift time of the detector, and to ensure that the electric field inside the accelerating tube is homogeneous - even with lots of ionized molecules inside it (space charge effects) - their total number should be small. By experience, it is known that the working pressure stated above avoids this problem. Furthermore one can remove water from the sample by cooling it below its melting point (but keep above the melting point of water) and then evacuate it, so that the number of "uninteresting" water ions is kept low.

2.5 Frequency Resolved Optical Gating

Frequency Resolved Optical Gating (FROG) is a technique to characterize a given laser pulse and retrieve the electric field $E(t)$. It is described in detail in [10, 13]. This is useful on a daily basis for checking the pulse duration out of the amplifier as well as for analyzing the pulses generated by the pulse shaper. We use a second harmonic generation FROG (SHG-FROG). It basically works as a Mach-Zehnder-Interferometer, with one variable arm length, and a second harmonic crystal at the intersection position. The second harmonic generated light (sum frequency generation of both bemas) is then analyzed by a spec-

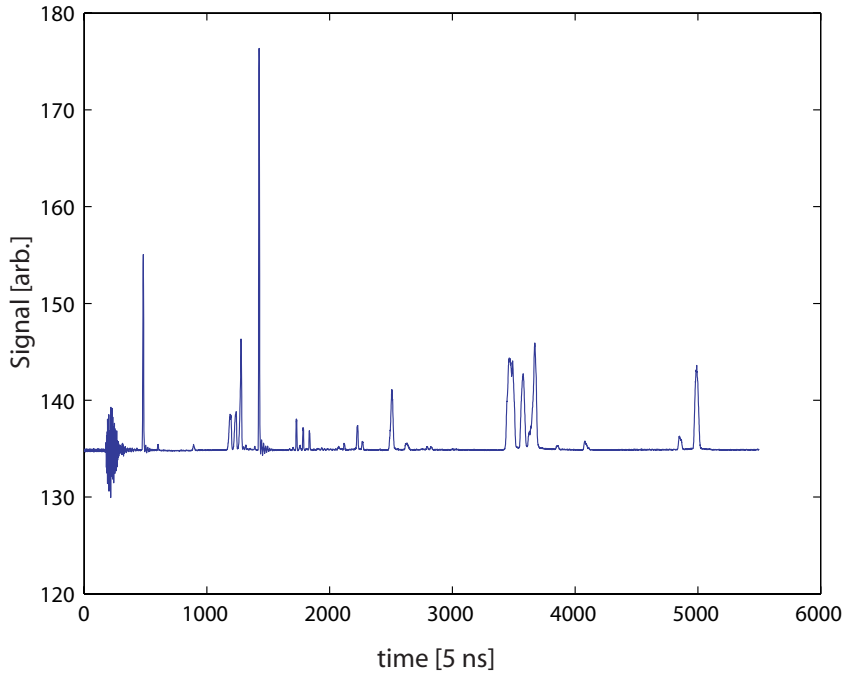

Figure 2.4 Example trace of the TOFMS of CH_2I_2, taken by the detector and the oscilloscope. It shows the TOFMS signal in dependence on the sampling point of the oscilloscope. The oscilloscope took sampling points at a frequency of 200 MHz. As the electric field is homogeneous one can infer from the flight time to the charge-to-mass ratio of the particles. Finally after re-calibrating the x-axis from time to charge-to-mass ratio, the peaks can be assigned to certain fragments.

trometer. Finally the FROG yields the Signal I_{sig} in dependence of ω and time delay τ (by varying arm length):

$$I_{sig}(\omega, \tau) = \left| \int_{-\infty}^{\infty} E(t)E(t-\tau)\, e^{\imath\omega t} dt \right|^2 \tag{2.1}$$

It can be proved that with an iterative algorithm the original electric field $E(t)$ is retrievable from $I_{sig}(\omega, \tau)$ (compare [38]). The absolute phase is not retrievable and the result is symmetric to time inversion.

2.6 The UV-Red setup

Some experiments have been also performed with mixed UV/red pump-probe scans. The complete UV setup is shown in figure 2.5.

The vacuum system itself (chamber, sample injection, and pumping) is constructed in the same way as the "old" setup described in chapter 2.1. Similarly the data acquisition software can be reused. So this chapter is constrained to describing the differences, i.e. UV femtopulse generation and solving several problems caused by different behavior of the optics for UV and red pulses.

The UV pulses are generated via frequency tripling. This setup is drawn in cartoon 2.6. The pulses first pass a beta barium borate crystal (BBO 1) to double the light to blue (390 nm) by second harmonic generation. A red beam with a power of about 900 μJ per pulse generates about 170 μJ blue

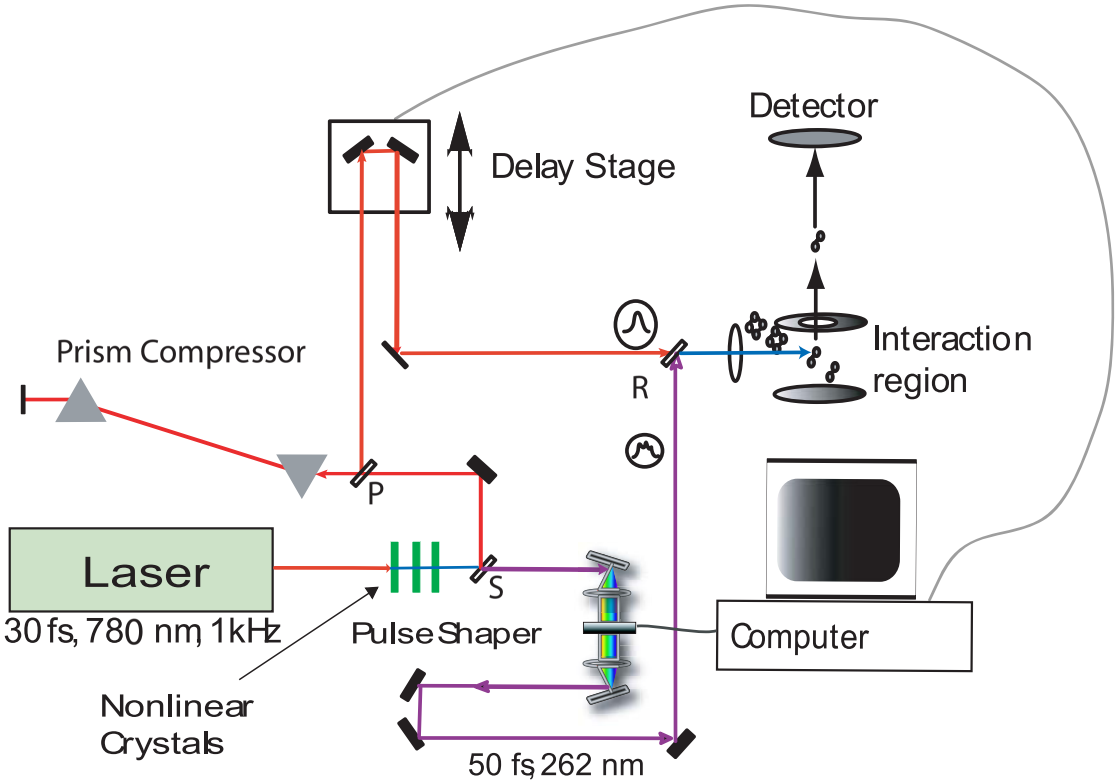

Figure 2.5 UV-Red setup: The red laser light is partly frequency tripled to UV by some nonlinear crystals and then split up via mirror S. The red pulses (780 nm) are compressed by removing group velocity dispersion (GVD) in the prism compressor. A reflection setup is used where each pulse passes the compressor twice and is finally picked up by a mirror P and then sent to the delay stage. The UV pulses (262 nm) are modulated by a pulse shaper. Both beams are finally recombined by the mirror R and focussed inside the chamber. The AOM in the pulse shaper, as well as the delay stage can be controlled by the lab software.

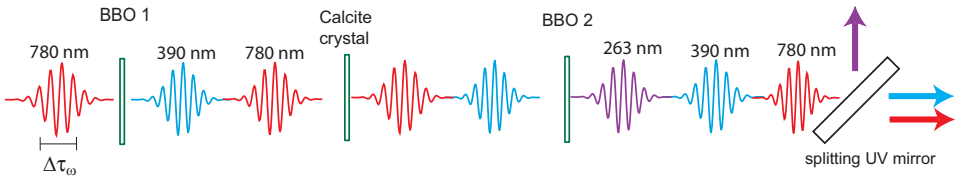

Figure 2.6 Red to UV tripling setup. First the red pulses are frequency doubled to blue pulses in the BBO crystal 1. The calcite window compensates for the phase difference between both pulses. In crystal BBO 2 blue and red pulses are mixed to generate UV light.

pulse light. The UV pulses are generated from the red and blue ones via sum frequency generation inside the second BBO crystal. Both beams are generated collinearly in the first crystal, but as they have different group velocities, the blue and red pulse do not overlap in time. Therefore a thin calcite crystal in between the two BBO crystals is used to compensate for that. So finally the beam consists of femtosecond pulses with central wavelengths of 780 nm, 390 nm and 263 nm. The maximum UV pulse intensity is about 8 μJ.

After the tripling part a fused silica mirror coated for UV reflection is used to split up both interesting components. As in the both beam lines only dielectric mirrors coated either for red or for UV reflection are used, the blue component quickly gets lost.

The red pulse passes the splitting mirror (fused silica, reflection coated for UV) unaffected, which is checked with the FROG and an unshaped pulse before. There is a convenient extension package of LabVIEW designed for ultrafast laser physics modeling [34]. Calculations with these show that the

red beam will have accumulated some chirp (of about $1000\,(\mathrm{fs})^2$) before it arrives at the chamber. To compensate for this, the beam is sent through a prism compressor, like it is described in section 3.1. It was decided to use a prism compressor instead of a compressor grating, which would have higher losses. The prisms can be aligned roughly at the Brewster angle and so have smaller reflection losses. With formula 3.4, the accurate spacing between both prisms can be calculated. The Fresnel Formulae predict (which is affirmed by a control measurement) a loss of 13%, which is considered tolerable. Finally the reflection mirror behind the second prism is tilted slightly, so that the reflected beam is not completely collinear with the incident beam, and can be separated by a pick-off mirror. Following the compressor, several mirrors are set to send the beam towards the delay stage. The UV beam then enters the UV pulse shaper after the splitting mirror. The mirror is constructed similarly to the red pulse shaper, as described in chapter 2.1 (or in full detail in [28]).

After the pulse shaper, the UV beam line is combined again with the red beam line. The same type of mirror as for separating both colors is used. A final lens with very short focal length (15 cm) focusses the beam inside the chamber. As the beam consists of two colors, the focal length for both components is different (about 2 cm) as well as their achromatic errors. To circumvent the latter problem a collinear setup is used and the beams are

sent through the center of the lens. To match the different focal lengths an additional slighting focussing lens system (about 2 m) is added to the red beam line.

Since both the red and the UV pulse have to arrive at the focal point at roughly the same time, the stage is moved to the "time-zero" position before each experiment, at which both beam lines are accurately of the same length.

For the adjustment on a daily basis, a similar procedure to the red setup is used (compare to section 2.3). The beam leaves the chamber through a second window and a focussing lens. This lens maps the focal point inside the chamber to a white card. Because of the different focal lengths for both colors, only the UV is in focus. Here the optimal position of UV spot is marked, for an optimal alignment. This helped to refind the optimal position. As both beams are collinear this also implies optimal alignment for the red beam and thus spatial overlap for both beams in the chamber.

For finding temporal overlap (time-zero), a BBO as used for sum frequency generation (BBO 2 in figure 2.5) is inserted after the chamber. After that, a prism splits the beam into its color components. Normally only a red and a UV spot are visible. But if and only if both pulses arrive at the same time, the BBO is able to generate blue light and a blue spot in between appears (the sum frequency mixing $red + blue = UV$ is the reverse effect to

the difference frequency mixing $UV - red = blue$). So the standard procedure to find temporal overlap for both pulses is to move the stage as long as a blue spot flashes.

Chapter 3

Ultrafast Optics

In the following chapter the theoretical background of some ultrafast optical effects is discussed, in sofar as it is needed for the described experiments and their interpretation.

3.1 Dispersion Control

Since all ultrashort pulses are simultaneously broadband wave packets, the control over their dispersion while passing through different materials is crucial. The overall dispersion is most easily described in frequency space. Therefore the spectral intensity $|G(\omega)|$ and spectral phase $\Phi(\omega)$ of a pulse are defined by

its electric field $E(t)$:

$$E(t) = \int e^{-\imath\omega t} G(\omega)\, d\omega \tag{3.1}$$

$$G(\omega) = |G(\omega)|\, e^{\imath\Phi(\omega)} \tag{3.2}$$

To describe the overall spectral phase of the pulse, it is expanded as a Taylor series (around the carrier frequency ω_0):

$$\Phi(\omega) = \phi_0 + (\omega - \omega_0)\phi_1 + (\omega - \omega_0)^2 \frac{\phi_2}{2} + \dots \tag{3.3}$$

with the expansion coefficients ϕ_k ($k = 1, \dots$); they are called the k^{th} order dispersion coefficients.

When the beam propagates through a material, the modification in its phase can easily be described by multiplication with a factor $H(\omega)$. Now the pulse has the overall spectral phase $\Phi(\omega)H(\omega)$. Because of the Fourier theorem this is equivalent to just adding the dispersion coefficients of the material to the spectral phase coefficients of the pulse.

ϕ_0 and ϕ_1 are the absolute phase and the group velocity of the pulse. As in our lab the pulse duration is 30 fs or longer, and the total beam length inside of transparent materials is small, we can restrict ourselves to controlling the amount of second order dispersion (or group velocity dispersion: GVD). A pulse with positive (negative) second order phase is called a positively (negatively) chirped pulse.

Since most materials add positive chirp to a pulse, special devices, like prism compressors or gratings, are used to remove the dispersion.

Figure 3.1 shows a schematic view of a prism compressor. The idea is to split up the beam into its different frequencies. Then the red light, which is ahead in time in a positively chirped pulse, is sent on a longer path than the blue components. The second prism is aligned antiparallel to the first one, so that it can recombine all components to one single beam again. As the red component has to cover a longer distance, it will lose some phase difference to the blue component. So this adds a negative chirp. A reflecting mirror directly after prism 2 can make the beam pass the setup a second time and so doubles the effect and reverses the spacing of the beam along the y-axis. By contrast to this negative chirp, the pulse has to travel through small pieces of glass inside the prisms, which adds some positive chirp depending on the material. In order to calculate the total amount of added chirp, both effects have to be taken into account.

If the second prism is moveable, one can vary the path length of the pulse inside the prism glass and thus its corresponding positive chirp. So the total additional chirp (positive, inside the prism and negative between them) is tunable. Reference [3] lists the correct formula for the added second order

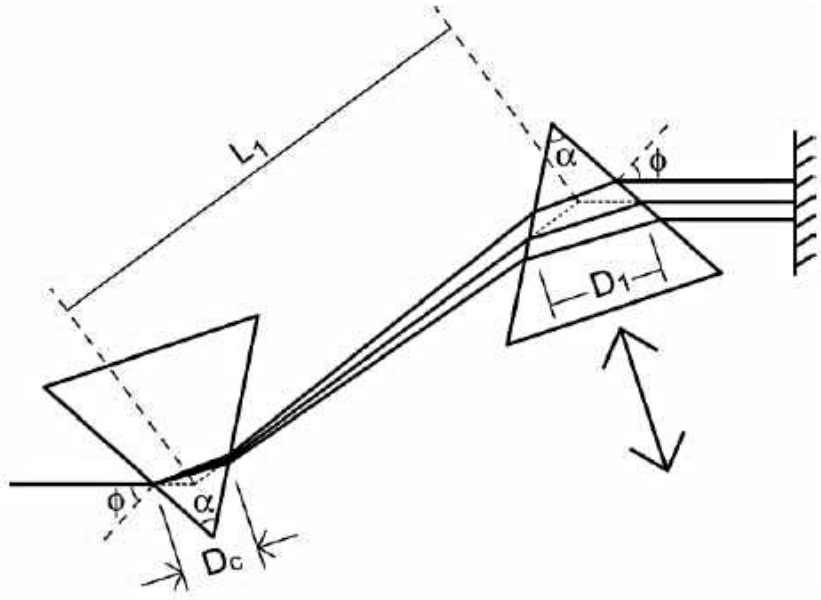

Figure 3.1 Schematic of a prism compressor made with a reflection mirror to double the beam path. Both prisms (ideally AR-coated) split and recombine the laser beam; as long as they are antiparallel they compensate each other exactly. The red light has a longer beam path than the blue, which corresponds to a negative chirp. But the short way inside the prisms ($\mathcal{D}_1$ and $\mathcal{D}_C$) adds a strong positive chirp to the pulse depending on their material. Its amount can easily be modified by moving the second prism in and out. (figure taken from [25])

dispersion. A sufficient approximative formula is:

$$\Delta\mathrm{GVD} \approx \frac{\lambda^3}{2\pi c^2}\left[\mathcal{D}\frac{d^2n}{d\lambda^2} - 4L_1\left(\frac{dn}{d\lambda}\right)^2\right]_{\lambda=\lambda_0} \tag{3.4}$$

where $\mathcal{D} = 2(\mathcal{D}_0 + \mathcal{D}_C)$ is the total path length inside the prism (for two bounces) and L_1 is the spacing between them. It can be seen that the overall added GVD splits up into a positive chirp of the prism medium itself (first summand proportional to $\mathcal{D}$) and the negative chirp for space between them (second summand, proportional to the spacing L_1).

3.2 Nonlinear optical effects

Nonlinear effects play an important role in ultrafast laser physics. Particularly in our lab: Kerr-lens modelocking in the Ti:Sapphire oscillator, SHG in the FROG, alignment for pump-probe experiments and frequency tripling for the UV generation.

In a medium the original electric field $\mathbf{E}$ of the incident beam is added to the electric field of the bound charges in the material. Therefore the electric displacement field $\mathbf{D}$, together with electric polarization $\mathbf{P}$ is defined as:

$$\mathbf{D} = \epsilon_0 \mathbf{E} + \mathbf{P}$$

In the simplest approach, the Lorentz model, the response of the electrons is linear: $\mathbf{P} = \epsilon_0 \chi \mathbf{E}$, with the material constant χ as the electric susceptibility. In this case $\mathbf{D}$ is linear in $\mathbf{E}$. But with increasing electrical field strength, the anharmonicity of the potential of the bound electrons results in a non-linear relationship between $\mathbf{P}$ and $\mathbf{E}$. In the general case, χ is dependent on $\mathbf{E}$, which can be described by a Taylor expansion (see [6]):

$$\mathbf{P} = \sum_n \mathbf{P}^{(n)} = \epsilon \sum_n \chi^{(n)} \mathbf{E}^n$$

In general the expansion coefficient $\chi^{(n)}$ is a tensor of rank $n+1$ (although I have suppressed indices for clarity). Obviously the first order term leads to the well known linear optical behavior.

Second harmonic generation and sum frequency generation are fundamental for the work described in this thesis, and most important for the generation of UV light (see 3.2). These two effects are caused by a non-vanishing $\chi^{(2)}$. For simplicity we restrict ourselves to two plain, linearly polarized, monochromatic waves with the frequencies ω_1 and ω_2, so that the total electric field is $E = E_1 e^{\imath\omega_1 t} + E_2 e^{\imath\omega_2 t} + \text{c.c.}$. Thus the above formula yields:

$$P^{(2)} = \epsilon_0 \chi^{(2)} E^2 \tag{3.5}$$

$$= \epsilon_0 \chi^{(2)} \left[E_1^2 e^{2\imath\omega_1 t} + E_2^2 e^{2\imath\omega_2 t} + \text{c.c.}\right] + \epsilon_0 \chi^{(2)} \left[2E_1 E_2 e^{\imath(\omega_1+\omega_2)t} + \text{c.c.}\right]$$

$$+ \epsilon_0 \chi^{(2)} \left[2E_1 E_2^* e^{\imath(\omega_1-\omega_2)t} + \text{c.c.}\right] + 2\epsilon_0 \chi^{(2)} \left[E_1 E_1^* + E_2 E_2^*\right] \tag{3.6}$$

Obviously the electromagnetic field inside the medium now contains also components of the frequency $2\omega_1$ and $2\omega_2$ (second harmonic generation), as well as $\omega_2 + \omega_1$ (sum frequency generation), $\omega_2 - \omega_1$ (difference frequency generation) and a constant field shift. The formula also yields that all these effects are proportional to the *product* of the involved electric fields. This means for the intensity of the second harmonic generated light $I_{SHG} \propto I_1 I_1$, and it follows for the intensity of the frequency added light : $I_{sum} \propto I_1 I_2$. However usually none or only one of these generated frequencies will be observable. The reason for this is the so called *phase matching condition*.

For example the second harmonic wave is always in phase with its fun-

damental at the place of its generation. But, as both waves have different phase velocities inside the medium, the second harmonic will (in general) be out of phase with the second harmonic generated at a different spot. If a non-vanishing output of frequency added light is desired, the phase matching condition has to be satisfied (with $\omega_3 = \omega_1 + \omega_2$):

$$k_1 + k_2 = k_3 \Leftrightarrow n_1\omega_1 + n_2\omega_2 = n_3\omega_3 \tag{3.7}$$

Figure 3.2 shows the quantum mechanical interpretation for the sum frequency generation. Two photons are absorbed to an intermediate level and one with ω_3 is emitted. From this point of view the frequency of the emitted photon is obviously the sum frequency in order to ensure energy conservation. In addition, momentum conservation directly yields the phase matching condition.

For isotropic media with normal dispersion, eqn. 3.7 can never be true, since $\omega_3 > \omega_2, \omega_1$ and $n_3 > n_2, n_1$. Theoretically phase matching can be achieved by using anomalous dispersion. But there is a much easier and more common way: Birefringent crystals naturally provide different indices of refraction for different polarizations. By carefully adjusting the crystal orientation, phase matching can be established.

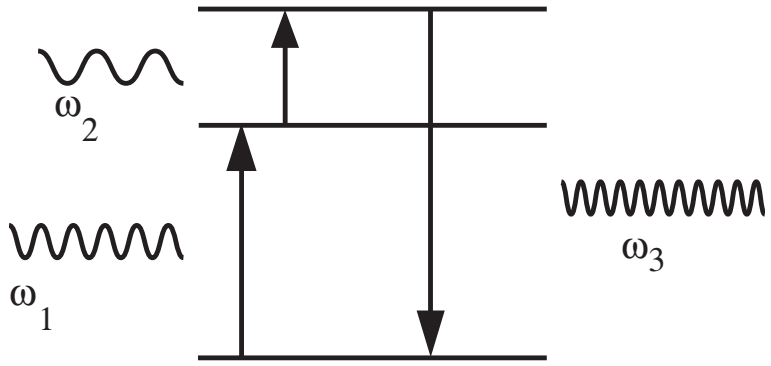

Figure 3.2 Sum frequency generation: One atom absorbs two photons of frequencies ω_1 and ω_2 and then emits only one photon ω_3 to drop again to ground level. Energy conservation leads to $\omega_1 + \omega_2 = \omega_3$ and momentum conservation to the phase matching condition: $k_1 + k_2 = k_3$.

3.3 Ultrafast coherent control and closed loop feedback with genetic algorithm

The topic of ultrafast coherent control covers a very broad field in physics. It centers around the idea of controlling optical, physical and chemical processes using coherence effects in matter by ultrafast lasers. A general overview is given in [33, 39], and some implementations are described in [7, 8, 32].

Shaped laser pulses can be used to modify the transition probability between two certain levels of a molecule. Particulary, this thesis discussed, if and by how much the Cl_2 and I_2 yield from CCl_4 and CH_2I_2 can be increased by

changing the pulse shape. Finding the ideal pulse shape is theoretically very difficult and easily surmounts available computing power. The experimental approach to this is to use a genetic algorithm (GA), as described in [2].

The basic idea is shown in figure 3.3. The GA is an iterative algorithm to find the optimal pulse shape starting with an unshaped pulse. The name is chosen in analogy to biological evolution. The goal is set in the GA software, to enhance the *fitness* of the signal. The fitness is a functional based on the detector signal, e.g. in the easiest case, just the total count of a certain ion. Similarly to evolution, each pulse shape is encoded in the software by its genes; normally 20 to 40 points, that give the desired phase of the laser pulse at certain frequencies. The complete pulse phase is given by an interpolation between these points.

Each generation starts with the optimal pulse shapes of the last generation. From these "parent" pulses the "child" pulses are generated by two operations: crossover and random variation, which resemble the biological processes of recombination and mutation. The first one hybridizes the genes from a pair of parents to generate the child genes. The second operation varies the genes randomly around the starting genes. The child pulses are finally written via the pulse shaper to the laser pulse and tested in the interaction cube on the sample. The GA calculates the fitness for each pulse and then selects the best

pulse shapes to be the parents for the next generation.

A graph showing the fitness versus iteration qualitatively looks like shown in figure 3.4. The fitness is staring to rise dramatically after a few iterations and finally saturates. It usually takes 50 to 100 iterations till the GA feedback converges to a pulse shape.

As the GA uses random elements, two questions arise: As to(a) about the reproducibility of the results and (b) if the algorithm really finds global optimal solutions, instead of local maxima. To (a), principally there can be an infinite number of optimal results. But at least in the experiments described in this thesis, the GA results are grouped into several classes: the trivial result (enhancing fitness by removing higher order dispersion, which causes a stronger signal) and sets of mutually similar non-trivial solutions. As to (b), there exist theoretical articles (like [30]) that prove that GAs are principally capable to find optimal global solutions, although they assume ideal conditions, that are far from practical situations: that there are no limits for the GA in search space, i.e. no limits in pulse power, pulse duration, phase manipulation, etc.

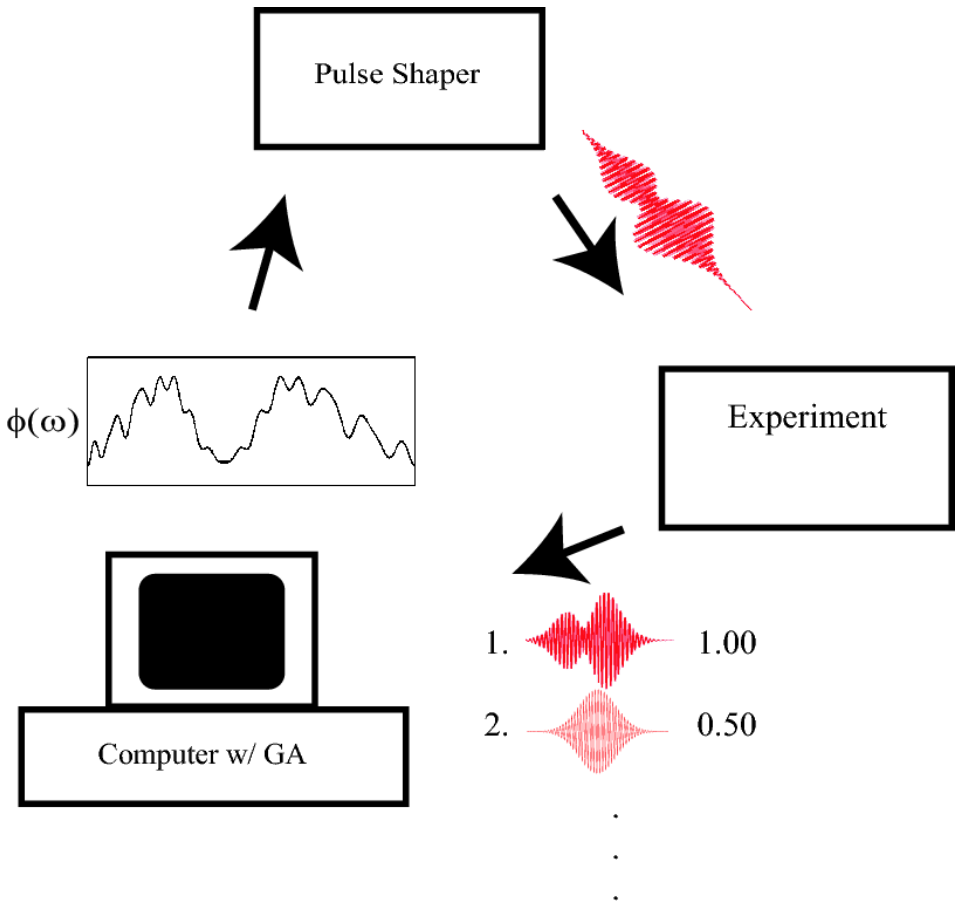

Figure 3.3 Closed loop learning control: A set of pulse shapes is randomly generated and written to the laser pulse by the pulse shaper. These pulses are used for the experiments. The detector signal is then used by the GA to calculate the effectiveness of the pulse. The best pulses are then the starting point for the next loop.

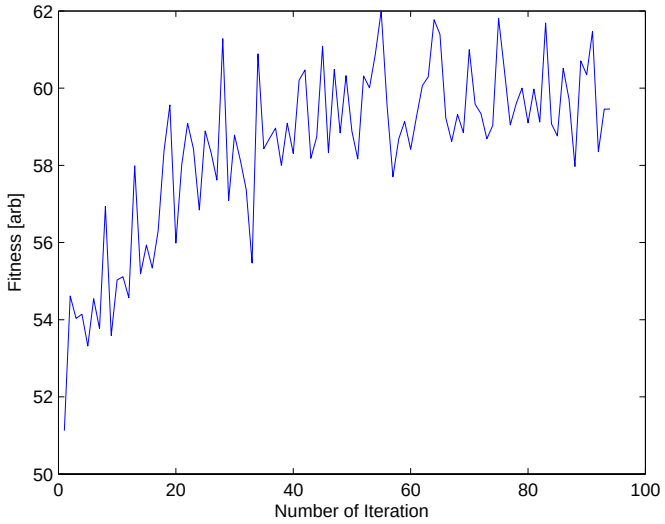

Figure 3.4 Qualitative evolution of the fitness (averaged over the top 8 pulse shapes) as a function of generation. (Here optimized for Cl_2^+out of CCl_4^+)

Chapter 4

CCl_4 experiments

The first molecule studied was Carbon-tetrachloride (CCl_4). We examined the laser driven reaction:

$$CCl_4 + nh\nu \rightarrow Cl_2^+ + \ldots \tag{4.1}$$

This was done for various motivations: First a former group member, D. Cardoza, detected Cl_2^+ while working with CCl_4. Also there are some papers (like [23] and [5]) observing this process under femtolaser excitation and to form Cl_2 (neutral or ionic) from CCl_4. The chemical structure of the molecule is shown in figure 4.1.

The goal of these experiments is to verify the results of other groups, to check if this process also produces chlorine ions, and if so, what the involved molecular levels are and if the Cl_2^+ yield can be controlled . For this purpose shaped single pulse experiments are performed in combination with a genetic

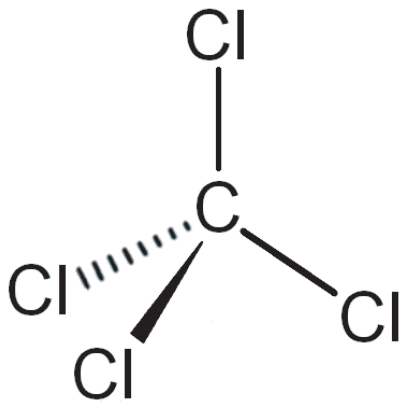

Figure 4.1 Schematic view of a CCl_4 molecule. It has a methane-like shape, whereby the hydrogen atoms are replaced with chlorine atoms.

algorithm.

4.1 General facts of the Cl_2 data

The sample had several non-ideal properties. It was naturally contaminated with Cl_2 from the very beginning on, both because of the way it is industrially produced (MP Biomediacls gives a purity of 99.9%), and because of the sensitivity of halogenated methanes to air and light. Once opened, the chemical aged and formed molecular chlorine inside the storage bin. Furthermore, there was contamination from former experiments in the chamber. Thus the measured yield of Cl_2^+ was only partly due to Cl_2^+ formed from CCl_4 by interaction with the laser. In order to determine what fraction of the mea-

sured Cl_2^+ was due to contamination we made measurement to estimate the Cl_2 contamination.

We found that approximately half of the detected Cl_2^+ is due to background. This make its an open question, whether the observed pulse shape depending behavior is due to the Cl_2^+ formed from CCl_4 or due to the background Cl_2.

There were two possible ways for estimating the number of Cl_2^+ in the chamber. The first was to use the TOFMS signal and the second one was to use a residual gas analyzer (RGA).

When the laser intensity was high enough, the signal of all fragments started to saturate (as a function of pulse energy), which was due to the fact that finally all molecules in the laser beam were ionized and fragmented in some way. This happened at about $200\,\mu$J, as can be seen in figure 4.2. In this case, each fragmented CCl_4 molecule produced exactly one ion that contained a C atom. The signal sum of $CCl_4^+ + CCl_3^+ + \cdots + C^+$ was proportional to the overall number of fragmented CCl_4 molecules inside the beam. So the sum signal of these fragments at a sufficiently high energy (when all these particles are already in the saturating regime) gave the number of CCl_4 molecules inside the laser focus (times a constant, that represents the detection efficiency). The exact value of this constant is not needed, as the detector sensitivity for each ion was equal and one only looked at relative signal.

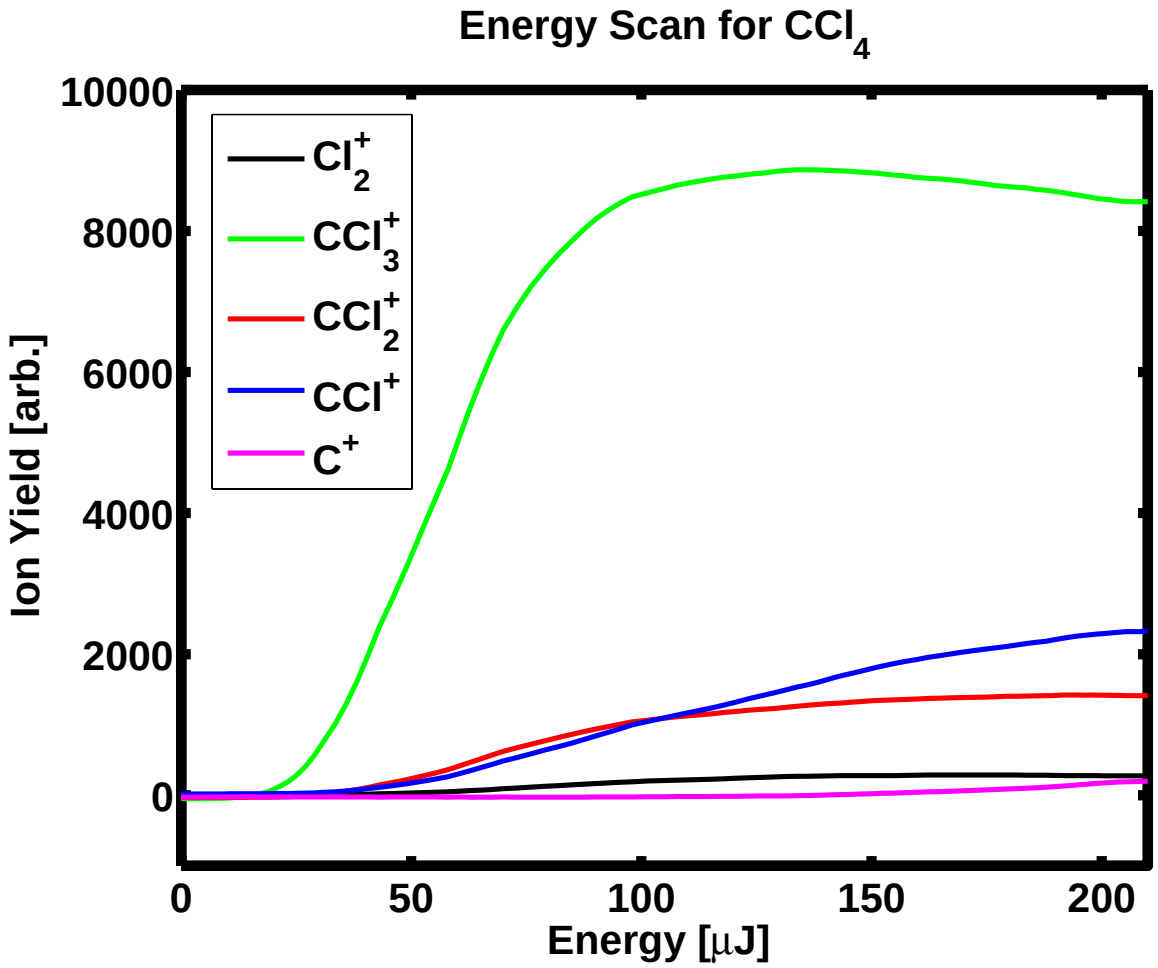

Figure 4.2 Ion yield (in arbitrary units) of fragmented CCl_4 for pulse energies from 0 to 210μJ: obviously CCl_3^+ has the biggest contribution. At the maximum energy 210μJ all fragments have started to saturate. Their values are: 8400 (CCl_3^+), 1400 (CCl_2^+), 2300 (CCl^+), 200 (both for C^+ and Cl_2^+)

Similarly the Cl_2^+ signal was a lower bound for the Cl_2 inside the beam, either formed by fragmentation or just ionized contamination. It was just a lower bound, as some Cl_2 was likely to be destroyed by the laser. For the example in figure 4.2 the situation for the highest pulse energy 210 μJ can be read. As CCl_4 has no stable parent ion, the CCl_4^+ signal is zero. So this leads to the following estimate:

$$\frac{N(\text{formed}Cl_2\text{and}\text{contamination})}{N(\text{parent}\text{molecules})} = \frac{200}{8400 + 1400 + 2300 + 200} > 1.62\% \tag{4.2}$$

A different approach is to use the RGA of one of the chambers. Since the parent ion is not stable, fragmented ions were observed just by ionizing CCl_4. The electron impact mass spectrum [21] affirmed that just ionizing it does not produce any Cl_2. So in this case Cl_2^+ was neither formed from the parent molecule nor destroyed by the laser, and the RGA just showed the partial pressure of the background chlorine. And again summing up over all fragments that contain a carbon gave the partial pressure of CCl_4. So by assuming that the sensitiveness for all particles is roughly equal, this leads to an estimate for the contamination:

$$\frac{N(Cl_2\text{contamination})}{N(\text{parent}\text{molecules})} \approx 0.8\% \tag{4.3}$$

This was below the lower bound (4.2). This clearly proves the formation of Cl_2^+ from CCl_4^+ by the laser.

But one has to consider that in the worst case half of the detected chlorine signal was due to contamination. In other words the signal from contamination Cl_2 was comparable to the signal from generated chlorine. Therefore we could not rule out that all GA results are not just background effects, although most likely effects from both contamination and newly formed Cl_2 were observed.

The most direct solution to this problem would have been to repeat all these experiment with pure Cl_2^+. Then we could have distinguished the signal from contamination or created Cl_2^+. But for several reasons, we did not perform these experiments. First a practical problem: Our vacuum system is built up to insert liquid samples and to work with its low vapor pressure. We would have had to construct a new vacuum setup for it and do this very carefully for security hazards. And second, there were worries about our system itself, as parts of the vacuum system, especially the turbo pump and seals, could be corroded. This has been the main reason for continuing with studying CH_2I_2, as I_2 is much easier to handle.

4.2 Genetic Algorithm Experiments

These experiments studied whether the Cl_2^+ yield can be increased by changing the shape of the pulse interacting with the molecule. Therefore a single red pulse was used and optimized by the GA. Figure 4.3 shows the TOFMS of

CCl_4 produced by an unshaped pulse. We fed back on the Cl_2^+ signal for a variety of pulse energies and GA parameters. In the naive approach the fitness functional of the algorithm was the total Cl_2^+ yield. But also the control over a normalized Cl_2^+ yield was examined, i.e. the quotient or difference to other fragments (with appropriate weight factors). As the parent ion is not stable, CCl_2^+ and CCl_3^+ were alternatives. The diverse runs found optimal solutions, that increased the Cl_2^+ yield up to 8.0% at maximal pulse energy (around $200\mu J$) and up to 100% for low energies (around $45\mu J$). Figure 4.4 compares the TOFMS signal of a shaped and an optimized pulse, taken at a pulse energy of $40\,\mu$J.

The most successful pulses were scanned by the FROG and their shape was reconstructed. An example is shown in shown in figure 4.5. A common feature of all optimal pulse shapes, even for different fitness functionals, was a three intensity peak structure, with linear phases during the peaks. The time distances between the peaks varied, but were always between 50 fs and 150 fs.

Furthermore, we examined the ratio of optimized Cl_2^+ yield to unshaped pulse Cl_2^+ yields in dependence of the pulse energy. This revealed the interesting behavior shown in figure 4.6. The effectiveness of the GA control seems to be energy dependent and shows a hyperbolic-like behavior. The relative difference in efficiency was highest for low pulse energies and decreased for

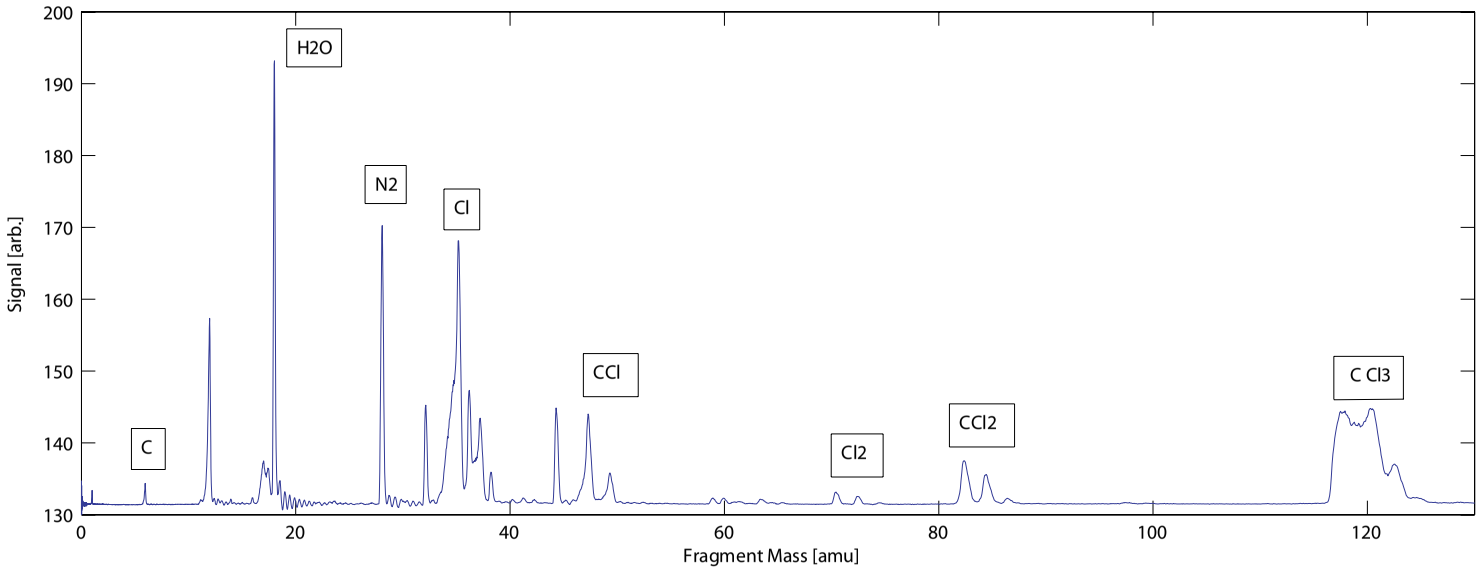

Figure 4.3 TOFMS of CCl_4at 220μJ pulse energy: The relevant peaks are labeled with the corresponding fragments. There is no CCl_4^+ peak, as the parent ion itself is not stable. Because of different Cl isotopes (35 amu and 37 amu), several ions have multiple peaks.

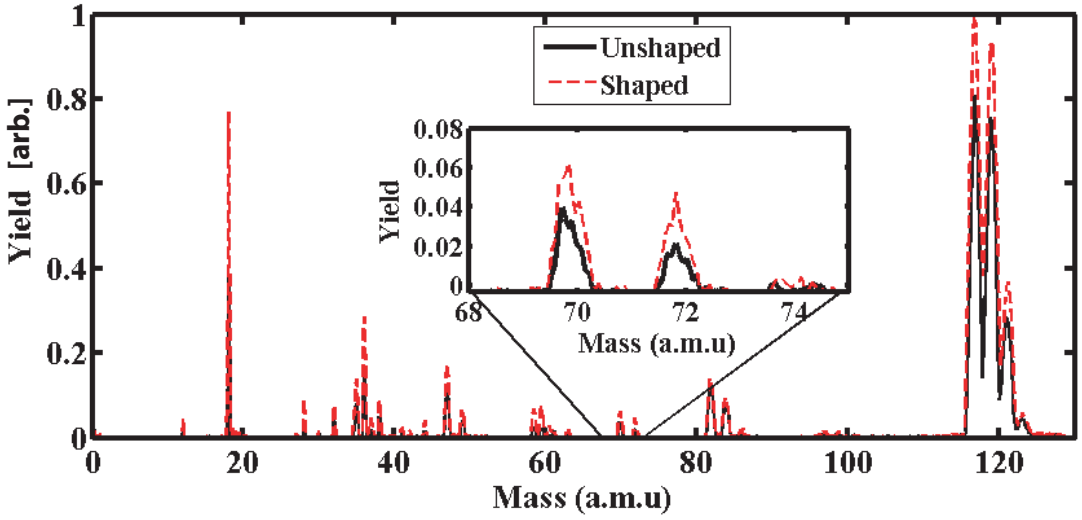

Figure 4.4 TOFMS of CCl_4 with an optimized pulse compared to an unshaped laser pulse at an energy of 40 μJ. The box zooms in to the interval of the Cl_2^+ signal. Here the Cl_2^+ signal is enhanced by about 70%.

higher energies. From a very pessimistic point of view this behavior could be just the GA increasing the pulse peak intensity (by removing higher order dispersion). This would be a trivial behavior and not of interest. But one can show that this effect is at least not the dominating effect: Otherwise, if there had been a significant amount of higher order dispersion, which the GA just had compensated for, this would have caused a constant factor for the ratio shaped/unshaped peak energy. According to graphic 4.7 some of the data was taken in a range of energy $70 \ldots 100\,\mu$J, in which the Cl_2^+ yield shows a linear dependence on the pulse energy. Thus, at least in this range, compensation of higher order dispersion would have contributed only a constant factor

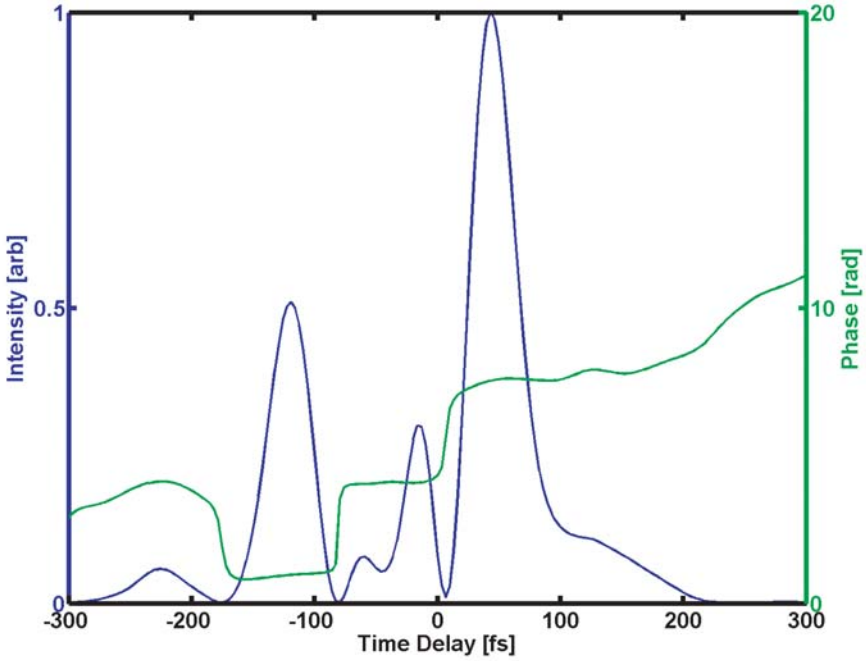

Figure 4.5 Example pulse shape with maximal Cl_2^+ yield: The pulse shape was measured with the FROG. The graph shows the temporal intensity (blue) and temporal phase (green). All optimal pulses had a three peak structure in common.

for all energies. As the graph 4.6 is obviously not constant in this interval ($70 \ldots 100\,\mu\mathrm{J}$), dispersion compensation could not be the main effect to cause this behavior.

The energy dependent efficiency of the GA indicated the presence of different mechanisms for producing Cl_2^+. With low energy, only few of these channels were possible and control over these (or only one of them) seemed to be easy and effective. With higher energies additional mechanisms became available, which responded in a different way to the shaped pulses. So finally the averaged effect on all channels together by the shaped pulse was less impressive. As described in section 4.1 it remained unclear if these different channels only comprise Cl_2^+ formation from CCl_4 or also include Cl_2^+ production from ionizing background Cl_2.

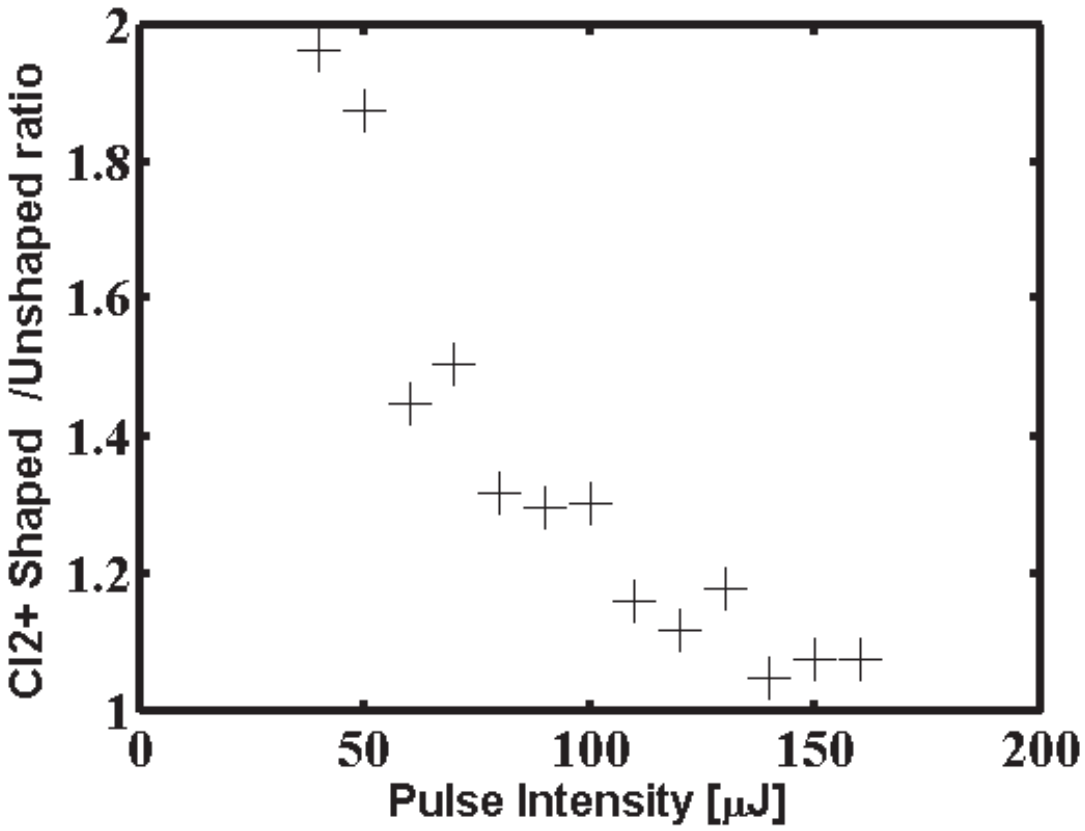

Figure 4.6 Relative Cl_2^+ yield of a GA improved shaped pulse to an unshaped pulse at different energies. The fitness functional was set to maximize the Cl_2^+ ion yield.

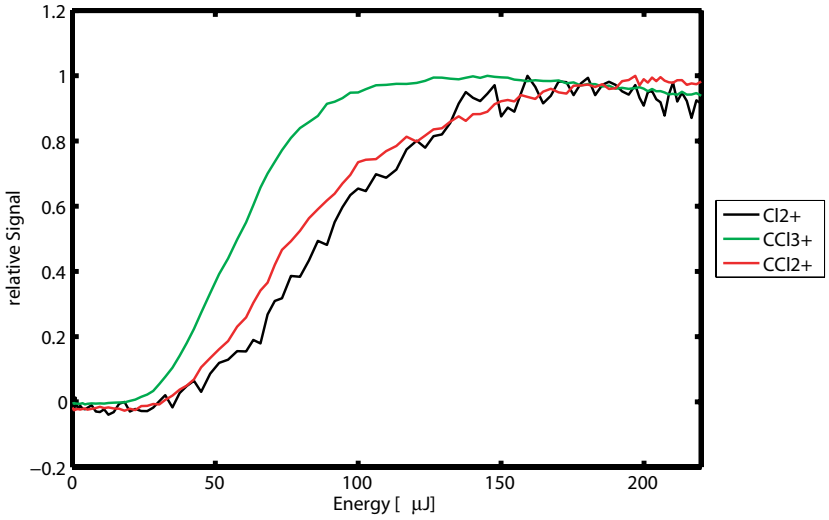

Figure 4.7 Energy scan of CCl_4: TOFMS signal of different fragments at different energies of the unshaped pulse: Cl_2^+(black), CCl_3^+(red), CCl_2^+(green). Each graph is normalized to 1 at its maximum. There is an almost linear dependence on energy in the Cl_2^+ signal between 70 μJ and 100 μJ

Chapter 5

Diiodomethane CH_2I_2 experiments

The CH_2I_2 experiments are the main experiments of my thesis. There are several papers that claim a similar behavior for CH_2I_2 to form I_2 under femtolaser excitation, like [23, 24, 43]. The article [44] especially deals with the possible underlying mechanisms for the concerted elimination of neutral I_2, and [26] shows that the efficiency of this process depends on the chirp of the pulse. [22] is of special interest as it explicitly addresses the contamination problem that has already occurred with CCl_4^+ and studies this reaction with a laser systems comparable to ours.

In addition, CH_2I_2 has several advantages to CCl_4. The generally weaker bonds of iodine to carbon than chlorine to carbon promise a more effective breaking process. Figure 5.1 shows the arrangement of the atoms in this molecule.

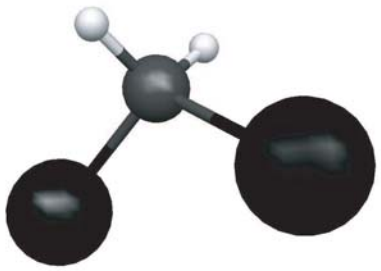

Figure 5.1 Structure of the CH_2I_2 molecule: The tetrahedron-like structure of methane is stretched due to the heavy (black) iodine atoms. The (grey) carbon atom is centered and bound to the (white) hydrogen atoms.

Generally CH_2I_2 samples suffer also from the same contamination problem as CCl_4, as they naturally contain molecular iodine. Similar to CCl_4 the sample ages when exposed to air and light, which increases the I_2 contamination. The first try with a commercially available sample affirmed this apprehension, as it contained about 1% molecular iodine. Luckily Professor Marecek from the Chemical Synthesis Center at Stony Brook University supplied us with a mostly iodine free sample. All experiments described in this chapter use this sample that is additionally stabilized with a copper wire, which binds molecular iodine chemically inside the storage bin.

A further advantage of this molecule is that iodine is much less aggressive than chlorine and solid at room temperature, which make it possible to perform control experiments with pure iodine, as I will present later. So finally in the next sections it will be demonstrated that it is possible to distinguish the iodine signal caused by contamination from the signal caused by iodine derived from $CH_2I_2$by this way.

Three types of experiments were performed with this molecule: (a) genetic algorithm experiments (similar to these with CCl_4) to examine, if it is possible to control the I_2^+ yield, (b) pump probe experiments with two red laser pulses and (c) pump probe experiments with a UV and a red pulse.

5.1 Genetic Algorithm experiments

This section will be discuss if the iodine yield from fragmentation of CH_2I_2 can be enhanced by different pulse shapes. These experiments are the counterpart to the GA experiments with CCl_4 described in chapter 4.

The ion yields of different fragments versus pulse energy (unshaped, transform limited pulse) are plotted in figure 5.2. With these numbers it is possible to roughly estimate the expected background iodine signal, similarly to the section about the chlorine contamination 4.1. If the laser pulse energy is high enough all molecules inside the laser field are ionized or even fragmented, which can be seen in the saturation of the signal with high pulse energy. In particular each excited CH_2I_2 molecule generates exactly one ion, that contains one C atom. So the total number of CH_2I_2 (times a constant corresponding to the detector sensitivity) in the interaction area can be estimated by adding all ion signals: C^+, CH^+, CH_2^+, ..., $CH_2I_2^+$. Reference numbers can be found in figure 5.2 at 210 μJ maximum energy, at which these fragments have reached the saturation yield. With the numbers given in this plot (the ion yield for CH and C is not shown but negligible), one can guess the total ion signal due to CH_2I_2 in the chamber is 7030.

The first commercial sample contains 1% iodine, as stated by its producer Acros Organics, which leads to an expected ion signal of 70 or lower from

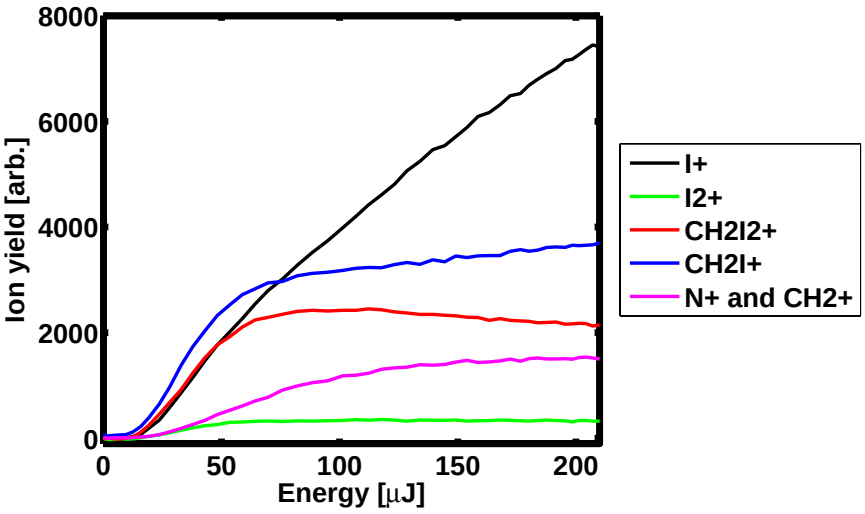

Figure 5.2 ion yield (in an arbitrary unit) of fragmented CH_2I_2 for (unshaped) pulse energies from 0 to 210μJ: At the maximum energy 210μJ all fragments have started to saturate. Their values are: 2170 ($CH_2I_2^+$), 3660 (CH_2I^+), 330 (I_2^+), 1500 (N^+ and CH_2^+).

iodine contamination.

Figure 5.2 also shows that the I_2^+ ion signal at maximum pulse energy is about 330, which is much more than the expected signal of 70 due to iodine contamination. This proves that at least 79% of the detected iodine is due to iodine formation from CH_2I_2. Background iodine ions contribute less than 21% to the signal. As the second sample, provided by Professor Marecek, is much cleaner, one could expect this contribution to be even lower.

The GA experiments themselves are performed in a similar way as the GA experiments with CCl_4. The algorithm is set to search for optimal solution for different fitness functions, like maximum I_2^+, or maximum ratios and differences

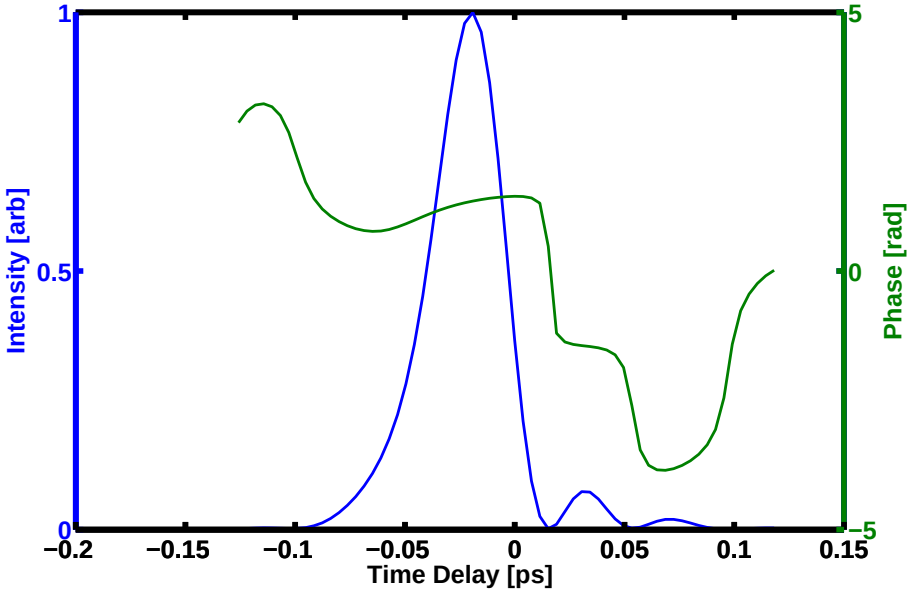

Figure 5.3 Optimal pulse shape for maximum I_2^+ with a CH_2I_2 sample. The shape of one main peak and several smaller ones following is characteristic.

to I_2^+ and other fragments ($CH_2I_2^+$, CH_2I^+, I^+). A typical GA enhanced pulse shaped is shown in figure 5.3 and can increase the iodine yield up to 12% compared to an unshaped pulse. All optimal pulses showed a similar behavior: One big intensity peak followed by a few smaller ones. The time difference between the first and second peak is about 55 fs, and between the following peaks about 40 fs. The phase is constant during an intensity peak and has jumps in between.

The significant amount of signal (21%) due to background I_2 raises again the question, whether the enhancement is due to more effective I_2^+ splitting from $CH_2I_2^+$ or due to more effective ionization of background iodine. Therefore

the same GA runs are repeated with a pure iodine sample. Indeed, the GA is able to improve the I_2^+ yield from a pure iodine sample. But its improvement does not surpass 8.3%.

Together with the information that the iodine contamination is at most 21%, it is fair to say that the iodine contamination contributes at most 1.7% to the total I_2^+ GA enhancement in the CH_2I_2 sample. This is an upper bound that is only reached, if the optimal pulse for I_2^+ formation from CH_2I_2 is at the same time an optimal pulse for background iodine ionization. This leaves an increase of at least 10.3% for I_2^+ formation from CH_2I_2.

So finally it can be concluded from this section that (a) I_2^+ can be formed from CH_2I_2 by laser excitation and (b) the efficiency of this process can be enhanced by at least 10.3% by modifying the pulse shape. It remains an open question whether this increase is significant and it is based on molecular dynamics rather than dispersion compensation. Eventually the pump-probe experiments described in the next chapter will provide more information on the internal molecular dynamics.

5.2 Red-Red pump probe experiments

The red-red pump probe experiments provide the main data of this thesis and the basis of the interpretation of the mechanism to form I_2^+ in chapter 6. The

preparations for the setup are described in section 2.1.

These measurements are made both with a CH_2I_2 sample as well as a pure I_2 sample in order to differentiate between laser driven concerted elimination and simply ionization of residual I_2 in our CH_2I_2 sample.

The most interesting piece of data is presented in figures 5.4 and 5.5. Both are color coded plots of ion yield for different fragments as a function of pump/probe delay and pulse energy. Note that the pulse, whose arriving time is varied, is the pulse with constant energy. This energy is kept constant at $110\,\mu$J for both scans shown. The arrival time of the pulse whose energy is varied is kept constant. The time difference between both pulses is varied from $-4000\,$fs to $4000\,$fs in $9.9\,$fs steps, which means that the pulses switch their role during the scan. The second pulse energy is varied from $0\,\mu$J to $100\,\mu$J, with a resolution of 21 steps. So on the left hand side the sample is pumped first with the strong $110\,\mu$J pulse and then probed with the energy varied second pulse. On the right hand side, the sample is pumped with the energy varied pulse first and then probed with the $110\,\mu$J pulse.

As both scans are taken at a long time scale and the vapor pressure of the pure iodine has not reached a equilibrium, these plots are already pressure corrected. Therefore the linear slope in the ion yields is subtracted.

Characteristically, all pump-probe scans show a strong time-zero peak.

This is due to overlap of pump and probe pulses and the nonlinear response of the molecules to the laser intensity. One could expect interference patterns, but both laser pulses have no fixed phase difference throughout the interaction region.

5.3 UV-Red pump probe experiments

Similar data was taken with a UV-red mixed pump-probe setup, as described in chapter 2.6. The result of the most interesting scan is plotted (pressure corrected) in figure 5.6.

Here the pump probe delay is varied again within the range from $-4000\,\mathrm{fs}$ to $4000\,\mathrm{fs}$ in $9.9\,\mathrm{fs}$ steps. The red unshaped pulse energy is kept constant during the whole scan at $55\,\mu\mathrm{J}$. The UV pulse energy is varied automatically from $0\,\mu\mathrm{J}$ to $1.4\,\mu\mathrm{J}$ in 100 steps.

Similar to the red pump-probe experiments, the original data shows a linear decrease in pressure. But due to leaks in the vacuum system between the sample holder and the reservoir at 3 times the pressure suddenly increases (once on the left side, twice on the right side). As it is known from former experiments in the group the water signal shows no time dependent dynamics, it is used as a indicator for the current pressure. So in this case the data is pressure corrected by normalizing it with a spline interpolation of the water

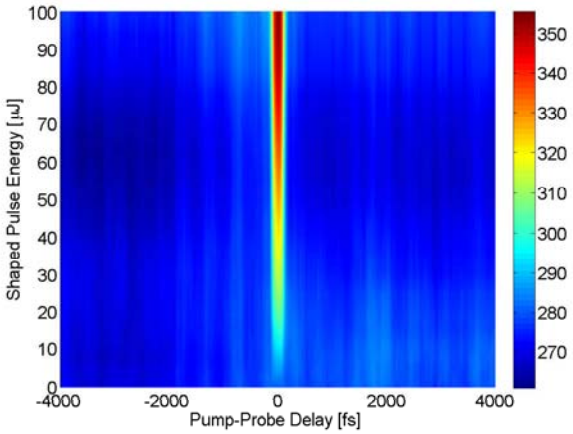

(a) H_2O^+ signal

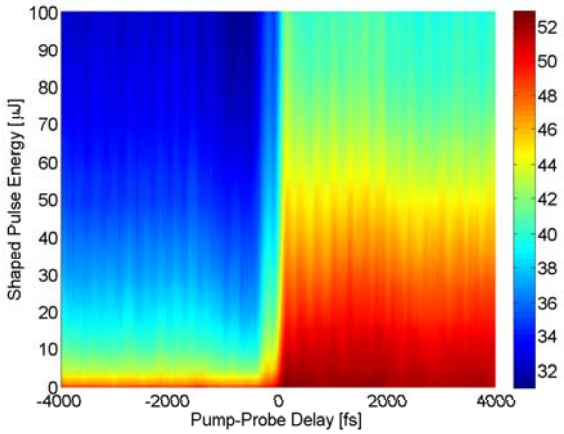

(b) I_2^+ signal

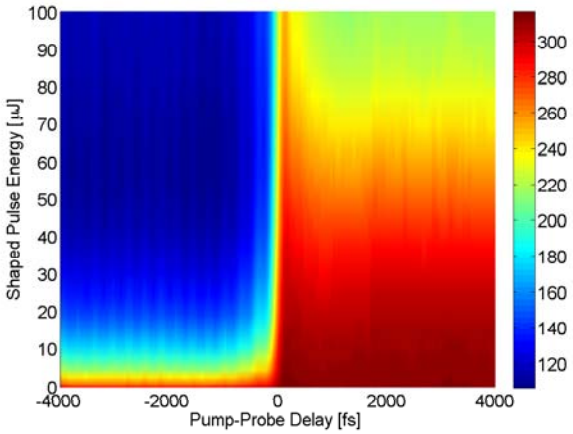

(c) $CH_2I_2^+$ signal

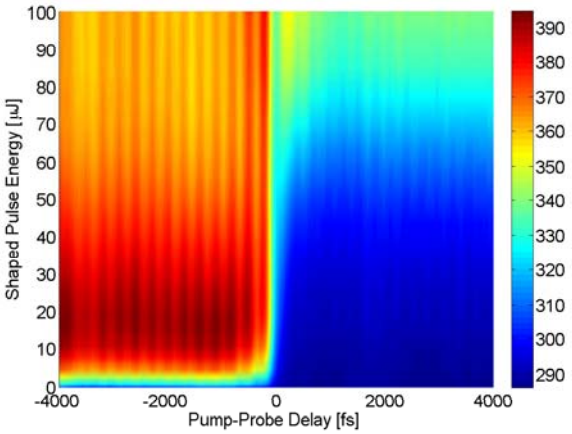

(d) CH_2I^+ signal

Figure 5.4 These figures show the ion yields for different fragments in a red-red pump-probe scan with a CH_2I_2 sample. The 2D-plot is color coded in dependency on the shaped pulse energy and time delay. On the left hand side the energy-constant 110 μJ pulse comes first, on the right hand side the energy-varied pulse comes first.

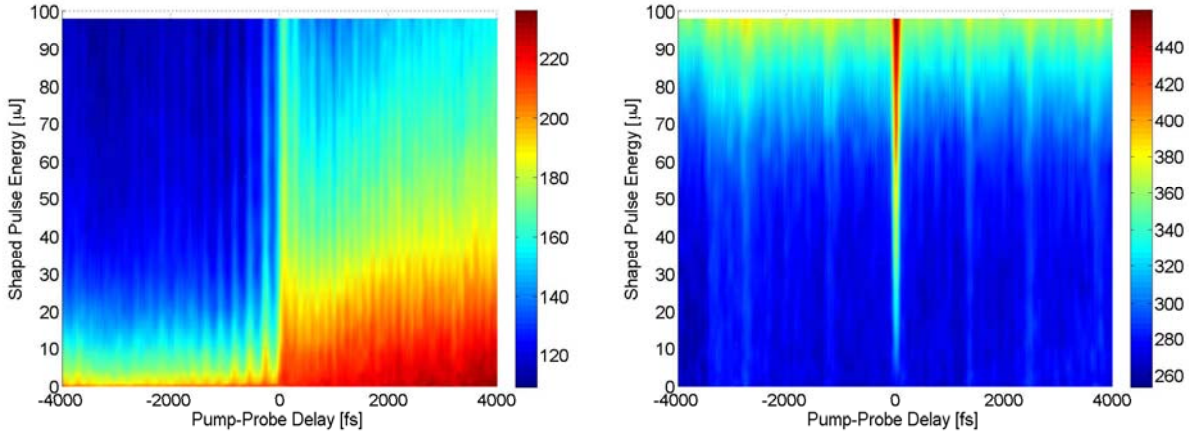

(a) I_2^+ signal

(b) H_2O^+ signal

Figure 5.5 These figures show the ion yields for different fragments in a red-red pump-probe scan with a pure iodine sample. The 2D-plot is color coded in dependency on the shaped pulse energy and time delay. On the left hand side the energy-constant 110 μJ pulse comes first, on the right hand side the energy-varied pulse comes first.

signal.

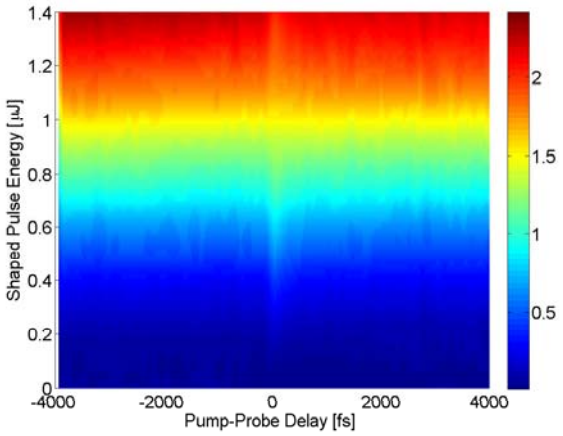

(a) H_2O^+ signal

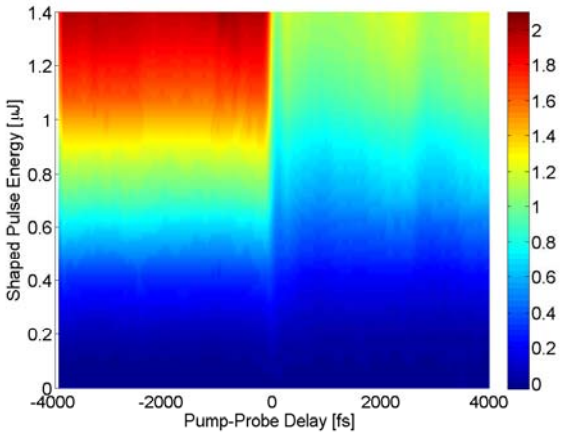

(b) I_2^+ signal

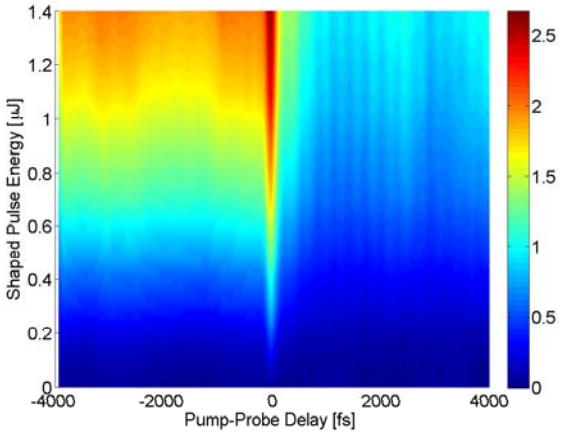

(c) $CH_2I_2^+$ signal

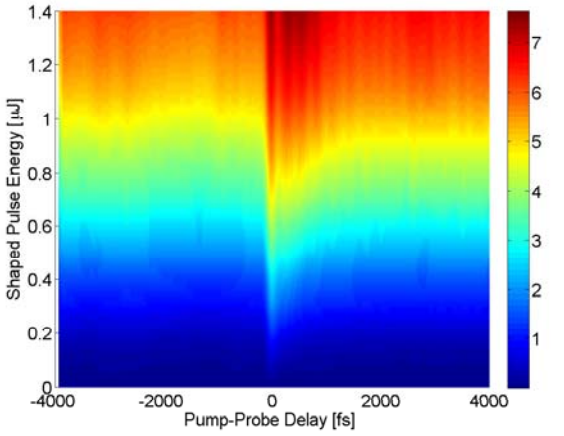

(d) CH_2I^+ signal

Figure 5.6 These figures show the ion yields for different fragments in a UV-red pump-probe scan with a CH_2I_2 sample. The red pulse energy is constant at $55\,\mu$J), the UV pulse energy is varied from $0\,\mu$J to $1.4\,\mu$J. On the left hand side the red pulse comes first, on the right hand side the UV pulse comes first.

Chapter 6

Discussion of the CH_2I_2 pump-probe data

In this chapter the pump-probe experiments, described in sections 5.2 and 5.3 are interpreted. With it the mechanism driving the I_2^+ emission from $CH_2I_2^+$ can be quantitatively resolved.

6.1 The oscillations in the ion yield

All pump probe scans (e.g. in the figures 5.4, 5.5 and 5.6) obviously show oscillations in the $CH_2I_2^+$, CH_2I^+ and I_2^+ signal. First of all, one can rule out technical causes (e.g. power fluctuations in the laser, detector signal processing), as this would affect the signal of all fragments. It is known from earlier experiments that the water signal does not to show any molecular dynamics, except the time zero peak. As it can be seen in 5.4(a), 5.5(b) and 5.6(a) the water signal behaves as predicted and is constant in time, except the usual

noise.

Thus the oscillations have to be caused by a time changing interaction behavior of the fragments themselves with the laser field. The molecule cannot be in an eigenstate of the field free Hamiltonian when it interacts with the second laser pulse. The eigenstates of each molecule can be characterized by electronic states, vibrational quantum numbers and rotational quantum numbers. [36] states time periods longer than 1.5 ps for rotational motion and $(20 \ldots 300)$ fs for vibrational excitation in CH_3I, which are roughly comparable to CH_2I_2. As CH_2I_2 has a larger angular momentum, one can expect the rotational motions to be even slower. So the timescale for rotational coherence is much longer than the observed oscillations. Finally electronic transitions happen on a sub-femtosecond timescale and thus are much to fast to be observed. This indicates that the observed behavior is due to a vibrational wave packet. Therefore these oscillations will be the key point to resolve the molecular dynamics.

6.2 The left hand side of the red-red data

The two sides of the pump probe scan shown in figures 5.4 and 5.5 demonstrate principally different behavior:

On the left hand side the pump energy is kept constant, whereas the probe

	ion yield [arb.]	$CH_2I_2^+$	CH_2I^+	I_2^+
LHS	mean (red 110 μJ - red 55 μJ)	34.6	100	9.75
	oscillations (red 110 μJ - red 55 μJ)	0.929	1.10	0.121
RHS	mean (red 55 μJ - red 110 μJ)	77.5	75.6	12.5
	oscillations (red 55 μJ - red 110 μJ)	0.851	0.283	0.160

Table 6.1 Ion yield and oscillation amplitude (in per cent of the CH_2I^+ yield on the LHS) of some fragments (averaged in time) for two red pulses red (55 μJ and 110 μJ) in different time order.

energy is varied. So the group of states accessed by the pump is constant, which leads to qualitatively constant dynamics in energy.

But on the right-hand side the pump energy is varied, the probe energy is kept constant. In this case different states are excited with varying the energy, which finally leads to different dynamics for different energies. This fact makes the right hand side more difficult to interpret.

Additionally, as it can be seen from table 6.1, the strongest oscillations are observed at the left hand side, with a first pulse (at fixed 110 μJ) and a weaker second pulse afterwards.

As this part of the data will be the most conclusive in interpreting the I_2^+ formation process and understanding the observed oscillations, the discussion will be focussed on it.

In order to take a closer look at the observed oscillations, some fragment signals are Fourier transformed along the time axis. They are plotted versus frequency (in wave numbers) and probe energy in panel 6.1. The frequency resolution is $\pm 4\,\mathrm{cm}^{-1}$.

This figure clearly demonstrates that the $CH_2I_2^+$, CH_2I^+ and I_2^+ derived from CH_2I_2 share oscillations at $111\,\mathrm{cm}^{-1}$. The I_2^+ signal in the CH_2I_2 sample shows two Fourier components: one at $111\,\mathrm{cm}^{-1}$, which is absent for probe pulse energies below $8\,\mu$J and a second at $130\,\mathrm{cm}^{-1}$, which is dominant at low probe energies. The I_2^+ signal from a pure iodine sample oscillates with $130\,\mathrm{cm}^{-1}$ at low probe energy. This contribution continually decreases in favor of a component oscillating at $121\,\mathrm{cm}^{-1}$ with increasing probe energy.

The fact that the Fourier spectra do not change in energy beyond $50\,\mu$J (see in fig. 6.1), neither in phase nor in amplitude (as it can be seen when the line outs are plotted separately), allows to average over the signals for this energy range. The result can be found in figure 6.2, where the ion yield versus pump-probe delay is drawn. The graphs are normalized in order to compare the yields for different fragments.

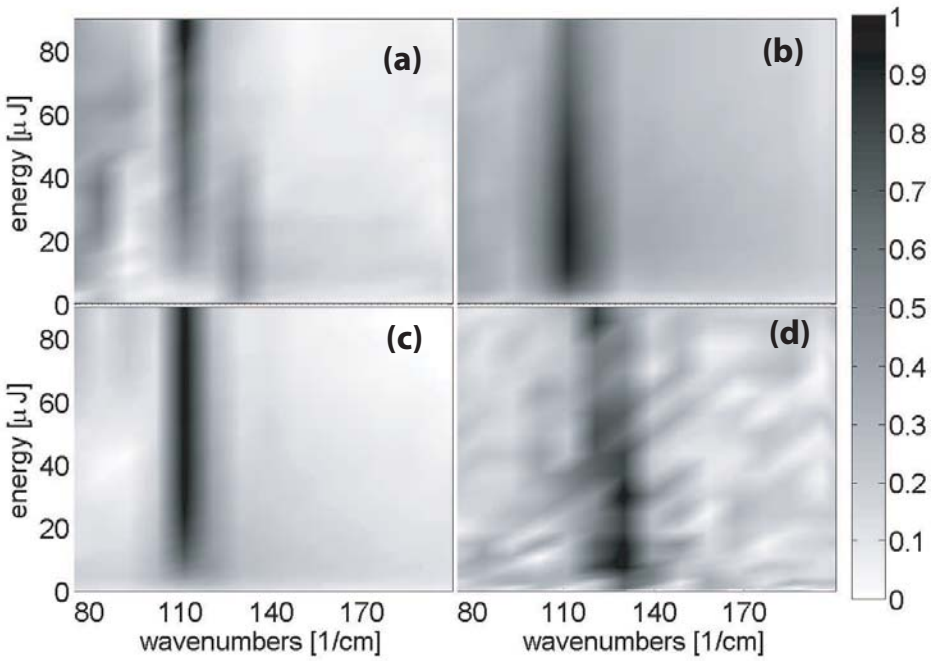

Figure 6.1 Panels: (a) I_2^+ (from CH_2I_2), (b) $CH_2I_2^+$, (c) CH_2I^+, I_2^+ (from I_2). They show the Fourier transformation (in time) of these fragment signals in a pump-probe scan, versus frequency and probe energy. The pump energy was constant at 110 μJ, the probe energy was varied from 0 μJ to 90 μJ in 21 steps.

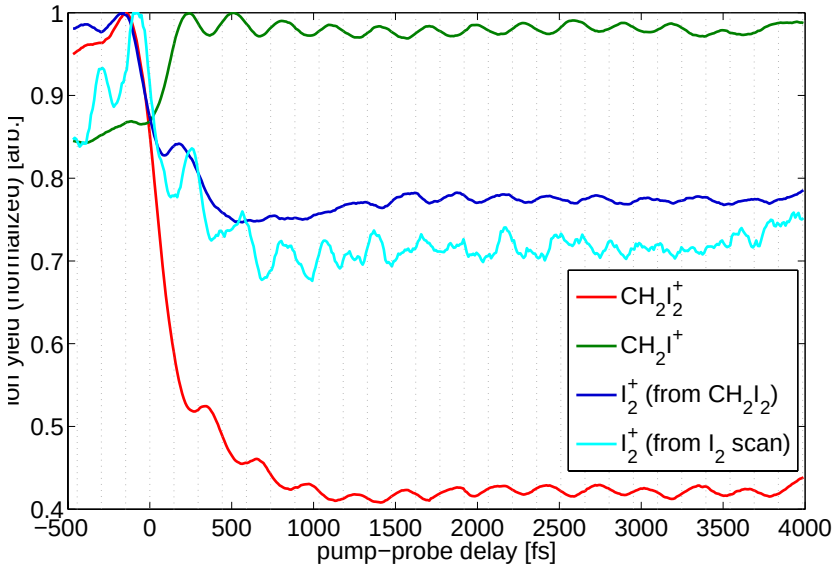

Figure 6.2 Normalized signal of several fragments versus delay time. Except the I_2^+ yield from $CH_2I_2^+$, all fragments are normalized to this interval, so that relative yields are invariant. The I_2^+ signal is enhanced by a factor of 10. Here the yields are averaged over probe energies from 50 μJ till 90 μJ. The dashed vertical lines have a spacing of 295 fs (which corresponds to an oscillation at 113 cm^{-1})

6.3 Frequency and phase of the oscillations

The pump pulse leaves the parent molecule in an excited intermediate state with one excited (or a superposition of several) vibrational modes. These will evolve in time, so that the transition probability of its atomic wave package to other molecular states after the probe pulse will vary with the pump-probe delay due to varying Frank-Condon overlap with the final state. The following paragraphs will discuss how the various yields are related and what motion leads to the modulation in the yields.

As already mentioned, CH_2I_2 suffers from the same contamination problem as CCl_4, although this time a much cleaner sample is used. Therefore it is an important first observation from the data that the I_2^+ signal for the CH_2I_2 sample behaves differently from the I_2^+ signal for a the I_2 sample. The control measurement with a pure iodine sample allows us to distinguish between contributions to our I_2^+ signal from contamination iodine (i.e. iodine which was formed in the sample prior to exposure with our laser pulses) from iodine formed by concerted elimination from CH_2I_2.

Reference [12] provides vibrational frequencies for various excited states of I_2, allowing to identify states of I_2 in which wave packet dynamics modulate the I_2^+ yield. The observed modulations at $130\,\mathrm{cm}^{-1}$ can be identified with wave packet oscillations in the $a^4\Sigma_u^-$ state in excited I_2^+ (the reference gives a

frequency of $(128 \pm 2)\,\mathrm{cm}^{-1}$ for this mode). This means for low probe energies, the I_2^+ signal (in the $CH_2I_2^+$ scan) seems to be dominated by wave packet oscillations in I_2^+ modulating its dissociation to I^+. (Consequently, the phase analysis of the I^+ signal shows anti-phased behavior with the I_2^+ modulations at low probe energy).

Towards higher pump energy the efficiency of destroying I_2^+ increases, so that these Fourier component continually fades. The paper also suggests a possible cause for the $121\,\mathrm{cm}^{-1}$ component: vibrational motion at $(125.7 \pm 2)\,\mathrm{cm}^{-1}$ in the $B^3\Pi_u$ state of I_2.

Most importantly, the $111\,\mathrm{cm}^{-1}$ component of the I_2^+ signal (in the CH_2I_2 scan) has no counterpart in the measurements with pure iodine. This is consistent with the observation of uncorrelated oscillations between both I_2^+ curves in figure 6.2. So it can be concluded that the oscillations at $111\,\mathrm{cm}^{-1}$ observed in I_2^+ above $8\,\mu$J probe energy are due to I_2^+ formed from CH_2I_2 coherently by our laser.

Before turning to a discussion of the molecular dynamics underlying the measurements, one can make one further observation. As it also can be seen in figure 6.2 by comparison with the sine reference curve (at $113\,\mathrm{cm}^{-1}$), not only the oscillation phases of each single fragment (in the CH_2I_2 scan) are constant, they are also mutually phase-locked. The phase of the modulations

in the $CH_2I_2^+$ and I_2^+ yields relative to zero pump-probe delay is π for a cosine oscillation (within the time resolution of our laser), whereas the phase of the modulations in the CH_2I^+ yield is zero (for a cosine oscillation).

As all fragment oscillations share a common frequency $111\,\mathrm{cm}^{-1}$ and are phase-locked, it indicates that the modulations are a result of wave packet motion in a single electronic state. If different potentials were involved, it would be very unlikely that they show such close vibrational frequencies (closer than $4\,\mathrm{cm}^{-1}$), which are additionally phase-locked. Furthermore neither our control scans with pure I_2 has shown any such oscillations for I_2^+, nor seem any close vibrations to be mentioned in literature for sure (compare to [12]). Figure 6.2 also demonstrates that the oscillations can be well explained by single sinusoidal signals. This points towards motion of a vibrational wave packet in a bound state with a nearly harmonic potential.

6.4 Potential energy surfaces

Table 6.2 lists all vibrational modes with their frequencies of the molecule, that involve at least one iodine atom.

The electronic ground state of the molecule can be ruled out as a reason for the observed oscillations. Within the given error range no frequency matches the observed oscillations. Furthermore, it is very unlikely that a large ampli-

Molecule \ Mode	I-C-I scissors	C-I_2 s.-str.	C-I_2 a.-str.
CH_2I_2	121[1] (127)	486 (486)	570 (568)
$CH_2I_2^*$	134	499	770
$CH_2I_2^+$	(113)	(537)	(503)
$iso-CH_2I_2$	C-I-I scissors 110 (97)	I-I stretch 128 (127)	C-I stretch 701 (733)

Table 6.2 Frequencies of all vibrational modes in CH_2I_2, $CH_2I_2^*$(both taken from [19]), $CH_2I_2^+$ and $iso-CH_2I_2$ (compare for both to [45]), that involve at least one iodine atom. All frequencies are given in wave numbers cm^{-1}. Theoretical results are written in brackets.

tude vibrational wave packet can be excited in the ground electronic state of the molecule under non-resonant excitation conditions.

This suggests to look for wave packet motion in an *excited* potential $CH_2I_2^r$. So far the experiment can be described best by a scheme like:

$$CH_2I_2(X) \xrightarrow{pump} CH_2I_2^r \xrightarrow{probe} I_2^+ + \ldots \tag{6.1}$$

$$\xrightarrow{probe} CH_2I^+ \ldots \tag{6.2}$$

$$\xrightarrow{probe} CH_2I_2^+ \tag{6.3}$$

It will be argued later that the $CH_2I_2^r$ in the intermediate step corresponds

[1]but [17] reports $127\,cm^{-1}$

to a low lying electronic state of the molecular ion. Figure 6.3 shows a cartoon of the relevant potentials. A vibrational wave packet is launched in the molecular ion through ionization. The subsequent elimination of CH_2I^+ and I_2^+ is driven by lifting the vibrational wave packet from the potential $CH_2I_2^r$ with the probe pulse to two different dissociative states, with control over which product is favored given by the timing of the probe pulse.

The fact that the CH_2I^+ and I_2^+ oscillations are anti-phased (π phase difference) indicates that the positions for an optimal branching ratio between CH_2I^+ and I_2^+ have to be close to the outer and inner turning points (B and A) of the potential. The fact that the phase of the CH_2I^+ modulations is zero (relative to zero pump-probe delay, i.e. CH_2I^+ emission has a maximum at time zero), indicates that the position for optimal branching ratio to CH_2I^+ (B), has to happen at the same reaction coordinate as the ground state minimum (C). One might wonder why the phases of the I_2^+ and $CH_2I_2^+$ signals are the same if the I_2^+ is being formed at the expense of $CH_2I_2^+$. Table 6.1 indicates that the amplitudes of the oscillations in the CH_2I^+ and $CH_2I_2^+$ signal are comparable but much stronger than the I_2^+ signal. This indicates that the maximum $CH_2I_2^+$ elimination takes place close to minimum CH_2I^+ production, which is again close to point A. Thus, the modulations in the $CH_2I_2^+$ are dominated by the formation of CH_2I^+rather than I_2^+, which is why the I_2^+ and

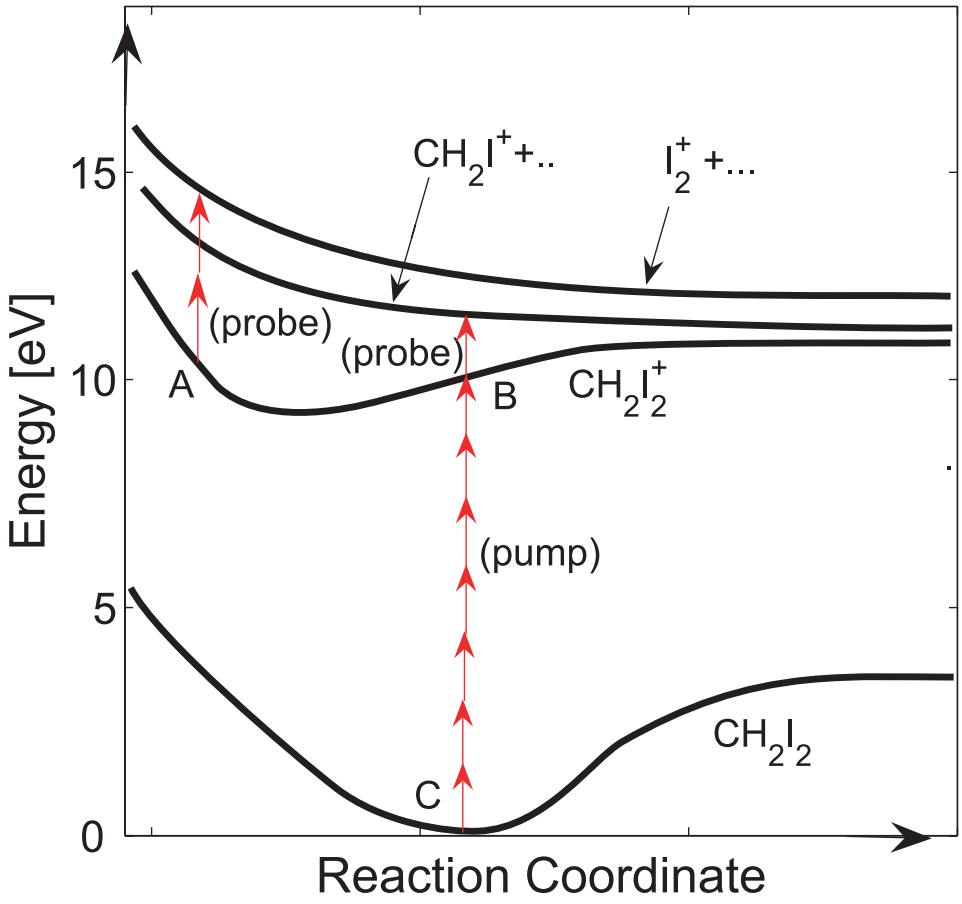

Figure 6.3 Cartoon of the involved potential energy surfaces in CH_2I_2. The pump pulse lifts the molecule from (C) to an intermediate state $CH_2I_2^r$ (in this cartoon $CH_2I_2^+$), that is shifted relatively to the ground state. This launches a wave packet in a one dimensional well. The wave packet oscillates between its inner turning point (A) and outer turning point (B). The absorption of one photon of the probe pulse can lift this wave packet from (B) to an dissociative level, that leads to CH_2I^+. From point (A) excitation by the probe pulse leads to dissociation with I_2^+ as a product.

$CH_2I_2^+$ yields are in phase.

6.5 Candidates for the intermediate state $CH_2I_2^r$

In this section the possibilities of the nature of that state $CH_2I_2^r$ and its vibrational mode causing the main frequency of $111\,cm^{-1}$ shall be discussed. First of all, an interval of possible energy difference between the ground state and $CH_2I_2^r$ can be given:

Plot 6.1 shows the oscillations have a different threshold for different ions. In figure 6.4 the oscillation amplitude at $111\,cm^{-1}$ of the different fragments is plotted in dependence on the probe pulse energy.

As one can see, the CH_2I^+ oscillations start immediately with any probe pulse energy, as well as the $CH_2I_2^+$ oscillations. The slope is linear for low energies. By contrast the I_2^+ oscillation begins after a threshold at about $8\,\mu J$. There are several theoretical and experimental articles, like [16] or [15], which examine what energy energy dependence can be expected depending on the underlying process. A general result is, that multi-photon absorptions always starts after a certain threshold of minimum intensity. This indicates that the I_2^+ formation is driven by one at least two photon absorption. Whereas the behavior of a immediate linear increase in ion yields from zero intensity shows that the transition from $CH_2I_2^+$ to CH_2I^+ has to be a single photon absorption.

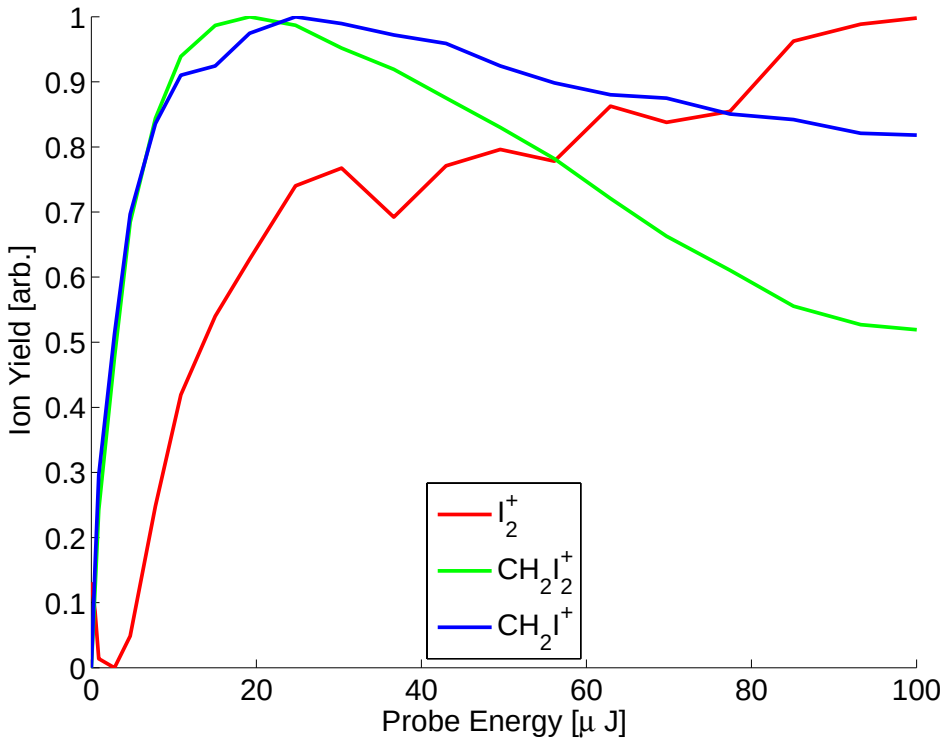

Figure 6.4 Ion yield of several fragments in dependence on the probe pulse energy. The signal is filtered by a narrow bandpass around 111 cm^{-1} and normalized, so that only the signal from ions that move through the intermediate state $CH_2I_2^r$ is counted.

(compare to [27])

Since CH_2I^+ can be formed via a single photon resonance by the probe pulse, the excited state where the wave packet evolves would have to be within 1.5 eV of the threshold for the formation of CH_2I^+ (10.46 eV [21]). Thus any excited electronic state $CH_2I_2^r$ in which the wave packet motion modulates the fragment ion yields must be at least 9 eV above the ground state.

Now several candidates for the state $CH_2I_2^r$ shall be discussed. Table 6.2 shows the vibrational frequencies of CH_2I_2, $CH_2I_2^+$, $CH_2I_2^*$iso $- CH_2I_2$.

6.5.1 Neutral states

That an excited neutral state is responsible for the oscillation seems to be unlikely. First because the derived energy restriction that it has to be at least 9 eV above ground level. And second, as the ionization potential is 9.5 eV, there is also a likely upper bound for the energy of neutral states. So all neutral states that are supposed to contribute to this oscillations are most likely in the range $9 \ldots 9.5$ eV.

Besides that, a neutral excited state of the molecule has the disadvantage that there are no excited state normal mode frequencies (or frequency differences) around $111\,\mathrm{cm}^{-1}$ for calculated neutral states (compare to table 6.2).

An interesting alternative to wave packet motion in the molecular ion or a

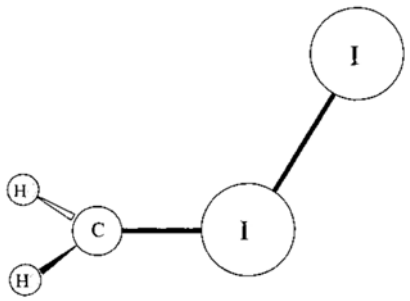

Figure 6.5 Molecular structure of Iso-Diiodomethane.

neutral state would be an isomerization of the molecule. It is know that CH_2I_2 can form $iso - CH_2I_2$ under laser excitation (see figure 6.5).

The expected frequency for C-I-I bending is $110\,cm^{-1}$ [45]. However, here it is also unlikely that this form of the molecule can be ionized by a 1.5 eV probe pulse photon and therefore this possibility is not considered to be realistic. Furthermore, there is some uncertainty in the frequency of this mode, with calculations yielding a frequency of $97\,cm^{-1}$ for C-I-I bending [45].

6.5.2 An excited ionic state

By contrast, the observations are consistent with wave packet dynamics taking place in the molecular ion. The presence of a high ion yield for zero probe pulse energy means that ionization is definitely taking place during the pump pulse,

but perhaps the most important argument in favor of this interpretation is the fact that the observed modulations match the I-C-I bend frequency calculated for the molecular ion (shown in table 6.2).

Additionally, the structure of the molecular ion yield is consistent with the wave packet dynamics occurring in a low lying ionic state. The I-C-I angle for the molecule is 97° in the ionic state [45], whereas the I-C-I angle for the neutral ground state is 116° [29]. The measurements thus lead to a very simple and intuitive picture of the dynamics leading to the formation of I_2^+. Due to this big displacement of equilibrium positions, the ionization of the molecule can launch a large amplitude bending wave packet which oscillates between large angles and smaller ones. The bending motion modulates the amount of I_2^+ and CH_2I^+ formed by the probe pulse. At the inner turning point both iodine atoms are close and tend to form an iodine molecule, at the outer turning point of this well, they tend to dissociate separately and form CH_2I^+. This associates the reaction coordinate in figure 6.3 with a monotonic function of the I-C-I binding angle.

6.5.3 Limits of the one-dimensional picture

So far only a one dimensional energy surface has been considered to explain the oscillations. Although it is natural that the bending motion along the I-C-I

coordinate influences the formation of I_2^+, this is clearly not the only motion influencing the production of I_2^+.

For example, there is a dramatic change in the ratios of the different ion yields between single pulse experiments (in figure 5.4 the line at $0\,\mu$J probe energy) and pump-probe experiments. Immediately following zero time delay between the pump and probe pulses, the $CH_2I_2^+$ and I_2^+ signals drop dramatically, while the CH_2I^+ signal increases complementarily, which indicates that one single probe pulse leaves a high amount of the parent molecule in an highly excited $CH_2I_2^+$ state, that easily can be lifted to CH_2I^+. The drop in I_2^+ signal is consistent with the molecular dynamics being dominated by dissociation of $CH_2I_2^+$ to form CH_2I^+. This corresponds to the picture described in the previous sections.

On the other hand, the amplitude of the observed oscillations do not modulate the total amount of $CH_2I_2^+$ lifted to CH_2I^+ between 0% and 100%. The oscillations are rather small (about 25% in figure 5.4), compared to the total change in the CH_2I^+ yield (between with and without probe).

So these large changes rather seem to take place on a multi-dimensional potential face, which includes other vibrational degrees of freedom, like the stretch modes. After the excitation to the ionic state the wave packet rapidly spreads on this surface, but keeps its shape along the I-C-I bending coordinate.

	$CH_2I_2^+$	$CH_2I_2^+$ oscillations	CH_2I^+	I_2^+
ion yield [arb.]	14.8	1.64	100	16.4

Table 6.3 Absolute ion yield (in percent of the CH_2I^+ yield) and oscillation amplitude of some fragments (averaged in time) for a UV pumped ($1\,\mu$J) and red probed ($25\,\mu$J) sample. The oscillation amplitude of I_2^+ and CH_2I^+ is not high enough compared to the background noise.

With sufficient dispersion no clear oscillations in the yields along the other coordinates, can be observed. The publication [27] deals with the analysis of this motion.

6.6 UV-Red pump-probe scan

The UV pump probe experiments will underline some of the results in the previous chapter. Here the UV pumped - red probed data is especially important (i.e. the right hand side in figure 5.6). Tables 6.3 summarizes the absolute ion signal of some relevant fragments at a UV pump energy of $1\,\mu$J.

In figure 6.6 several line outs for the main components I_2^+, $CH_2I_2^+$ and CH_2I^+ are plotted and normalized, corresponding to different UV pump energies. The big steps are due to some sudden pressure instabilities in chamber. But one can see, that at least $CH_2I_2^+$ shows oscillations that are mutually correlated for all of the energies shown. By contrast the background noise allows

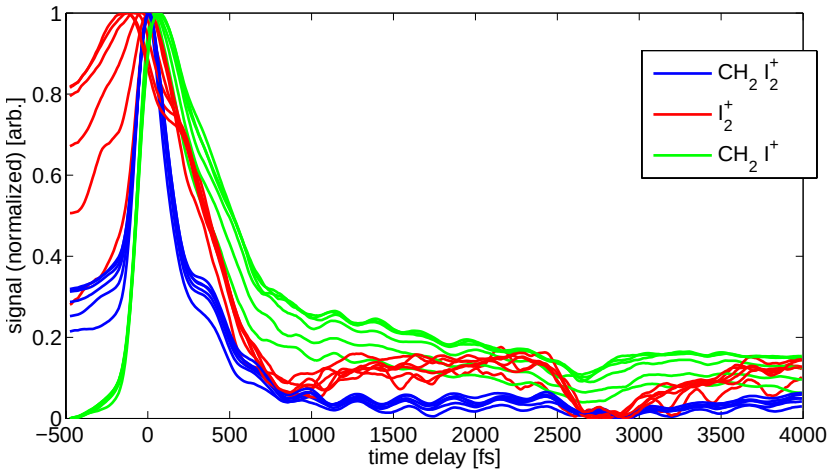

Figure 6.6 Normalized ion yields for several UV pump energies. Whereas the CH_2I_2 oscillations are correlated, the signals from CH_2I^+ and I_2^+ just seem to have random fluctuations.

no statement for I_2^+ and CH_2I^+.

A similar Fourier analysis to the red-red data, for the $CH_2I_2^+$ oscillations yields a frequency of $(108 \pm 5.5)\,\mathrm{cm}^{-1}$, that is in phase with the time zero peak (see figure 6.7), i.e. shows a maximum at zero delay. There are no higher harmonics, which indicate a pure cosine oscillation.

The observed frequency matches the frequency in the red scans within their error bars (see plot 6.1), but the phase is completely different to the red pumped oscillations in the previous sections.

Furthermore, if one compares the absolute ion yields from both the red-red (in table 6.1) and the UV-red (in table 6.3), the UV excitation shows

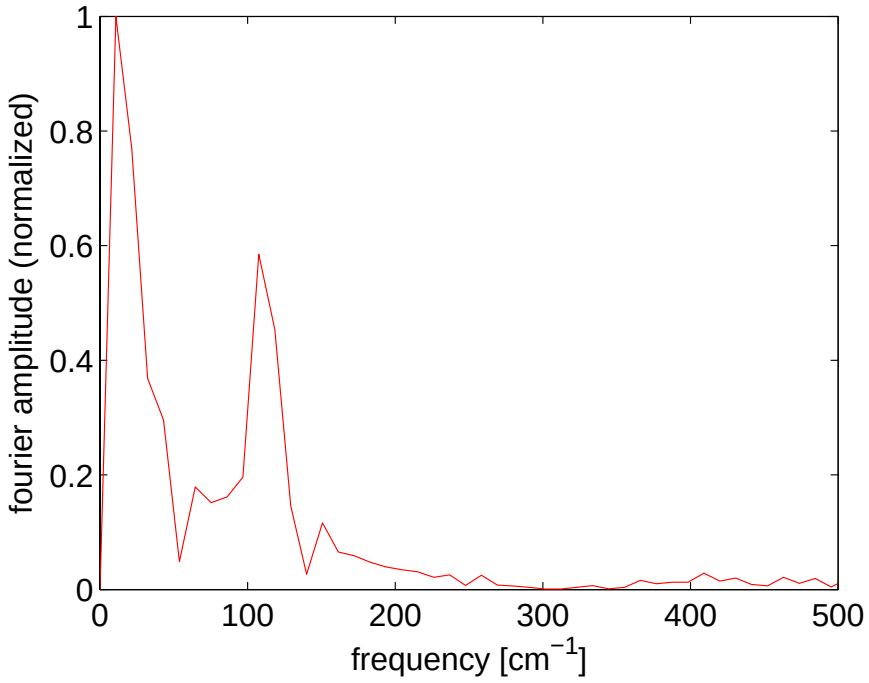

Figure 6.7 Normalized Fourier transform of the UV pumped $CH_2I_2^+$ signal: Besides the DC components the signal shows only one large peak at $108\,\mathrm{cm}^{-1}$.

different branching ratios. By contrast to the red data, the I_2^+ and CH_2I^+ yields are larger than $CH_2I_2^+$ signal. The oscillation amplitude in $CH_2I_2^+$ is also increased, whereas the oscillations in CH_2I^+ (which are comparable to the $CH_2I_2^+$ oscillations in the red-red scans) drop below the noise level.

These observations support vibrational motion happening in a different state, i.e. the iso-state discussed in section 6.5.1, which is much more likely to be formed in the UV regime. But further analysis and experiments will be needed to identify the involved potential and vibrational modes.

Chapter 7

Conclusions

The topic of this thesis is the concerted elimination of halogen molecules from halogenated methanes. Two model systems are examined: Cl_2^+ elimination from CCl_4 and I_2^+ production from CH_2I_2.

The formation of Cl_2^+ from CCl_4 is studied by single pulse GA experiments. They prove the possibility of driving this reaction under femtosecond laser excitation. The optimal pulse shapes can increase the Cl_2^+ yield up to 100%. The control seems to decrease with higher energies. Unfortunately the contamination with Cl_2 is too high to rule out background effects. Thus it remains as an open question to what extend these GA improvement are based on Cl_2^+ formation from CCl_4 or increased ionization of background Cl_2.

Diiodomethane CH_2I_2 is studied as the second model molecule. The GA approach is repeated. Additionally, pump probe experiments with two red

pulses and mixed UV and red pulses are performed. Several experiments are repeated with pure I_2 such that background effects can be ruled out. The GA algorithm is able to find pulse shapes that increased the I_2^+ yield from CH_2I_2 by up to 10%.

The red-red pump probe scans allow us to resolve one process that leads to I_2^+ concerted elimination from CH_2I_2. Based on these observations we can suggest a potential energy scheme (cartoon 6.3) to describe the dynamics. The molecule is excited to an ionic state launching a vibrational wave packet. This vibrational wave packet modulates the preferred decay channel to I_2^+, CH_2I^+ or $CH_2I_2^+$ by probe excitation. We suggest an one-dimensional well and can identify the excited mode with the I-C-I bending. When the wave packet is close to its inner turning point a two or more photon absorbtion can lift it to a dissociative level, that finally leads to the I_2^+ production. Close to the outer turning point, the laser pulse drives a one photon excitation that causes the CH_2I^+ formation.

Alternative intermediate sates and modes are discussed, a highly excited neutral state and iso $-$ CH_2I_2. Based on our observations, we can restrict the most likely energy interval of these states to $9 \ldots 9.5\,\mathrm{eV}$.

Interestingly the molecule shows a different behavior under UV excitation, which indicates dynamics in a different excited state.

Bibliography

[1] Z. Amitay, J.B. Ballard, H.U. Stauffer, and S.R. Leone. Phase-tailoring molecular wave packets to time shift their dynamics. *Chem. Phys.*, 267:141, 2001.

[2] A. Assion, T. Baumert, M. Bergt, T. Brixner, B. Kiefer, V. Seyfried, M. Strehle, and G. Gerber. Control of chemical reactions by feedback-optimized phase-shaped femtosecond laser pulses. *Science*, 282:919–922, 1998.

[3] Sterling Backus, Charles G. Durfee III, Margaret M. Murnane, and Henry C. Kapteyn. High power ultrafast lasers. *Review of Scientific Instruments*, 69(3):1207–1223, 1998.

[4] R. Bartels, S. Backus, E. Zeek, L. Misoguti, G. Vdovin, I. P. Christov, M. M. Murnane, and H. C. Kapteyn. Shaped-pulse optimization of coherent emission of high-harmonic soft x-rays. *Nature*, 406:164–166, 2000.

[5] V. R. Bhardwaj, F. A. Rajgara, K. Vijayalakshmi, V. Kumarappan, and D. Mathur. Dissociative ionization of gas-phase chloromethanes by intense fields of picosecond and attosecond duration. *Physical Review A*, 1998.

[6] Robert W. Boyd. *Nonlinear Optics*. Academic Press, San Diego, 2002.

[7] T. Brixner, B. Kiefer, and G. Gerber. Problem complexity in femtosecond quantum control. *Chem. Phys.*, 267:241–246, 2001.

[8] Paul Brumer and Moshe Shapiro. Coherence chemistry: Controlling chemical reactions with lasers. *Acc. Chem. Res.*, 22(12):407–413, 1989.

[9] Marcos Dantus and Vadim V. Lozovoy. Experimental coherent laser control of physicochemical processes. 104:1813–1859, 2004.

[10] R. Trebino J. Hunter DeLong, K. W. and W. E. White. Frequency-resolved optical gating with the use of second-harmonic generation. *J. Opt. Soc. Amer. B.*

[11] Kun Wu et al. Subfemtosecond pulse generation by cascade-stimulated raman scattering with modulated raman excitation. *J. Phys. B*, pages 349–355, 2003.

[12] L. Fang and G. N. Gibson. Investigating excited electronic states of I_2^+ and I_2^{2+} produced by strong-field ionization using vibrational wave packets. *Physical Review A*, page 063410, 2007.

[13] David N. Fittinghoff, Jason L. Bowie, John N. Sweetser, Richard T. Jennings, Marco A. Krumbugel, Kenneth W. DeLong, Rick Trebino, and Ian Walmsley. Measurement of the intensity and phase of ultraweak, ultrashort laser pulses. *Opt. Lett.*, 21(12):884–886, 1996.

[14] A. Flettner, J. Günther, M.B. Mason, U. Weichmann, R. Düren, and G. Gerber. *App. Phys. B*, 73:129, 2001.

[15] S. M. Hankin, D. M. Villeneuve, P. B. Corkum, and D. M. Rayner. Intense-field laser ionization rates in atoms and molecules. 64(1):013405, Jun 2001.

[16] S.M. Hankin, D.M. Villeneuve, P.B. Corkum, and D.M. Rayner. Nonlinear ionization of organic molecules in high intensity laser fields. *Phys. Rev. Lett.*, 84:5082, 2000.

[17] Max M. Heckscher, Leonid Sheps, Dieter Bingemann, and F. Fleming Crim. Relaxation of the c–h stretching fundamental vibrations of CHI_3, CH_2I_2, and CH_3I in solution. *Journal of Chemical Physics*, 117(19):8917–8925, 2002.

[18] J. Itatani, J. Levesque, D. Zeidler, H. Niikura, H. Pepin, J. C. Kieffer, P. B. Corkum, and D. M Villeneuve. *Nature*, 432:867, 2004.

[19] Wai Ming Kwok and David Lee Phillips. Solvation and solvent effects on the short-time photodissociation dynamics of CH2I2 from resonance raman spectroscopy. *J. Chem. Phys.*, 104:2529–2540, 1996.

[20] F.R. Langhojer. Toward understanding closed loop learning control: The importance of basis in searching the phase space, 2004.

[21] S.G. Lias. Ionization energy evaluation. In P.J. Linstrom and W.G. Mallard, editors, *NIST Chemistry WebBook, NIST Standard Reference Database Number 69*. National Institute of Standards and Technology, Gaithersburg MD, 20899, March 2003. http://webbook.nist.gov.

[22] Zhen-Hong Liu, Yan-Qiu Wang, Jian-Jun Ma, Li Wang, and Guo-Zhong He. Concerted elimination of CH_2, I_2 and CH_2ICl under intense femtosecond laser excitation. *Chemical Physics Letters*, pages 198–202, 2004.

[23] Una Marvet, Emily J. Brown, and Marcos Dantus. Femtosecond concerted elimination of halogen molecules from halogenated alkanes. *Phys. Chem. Chem. Phys.*, pages 885–891, 2000.

[24] Una Marvet and Marcos Dantus. Femtosecond observation of a concerted chemical reaction. *Chemical Physics Letters*, 256:57–62, 1996.

[25] P.H. Nuernberger. Design and construction of an apparatus for the neutral dissociation and ionization of molecules in an intense laser field, 2003.

[26] Igor Pastirk, Emily J. Brown, Qingguo Zhang, and Marcos Dantus. Quantum control of the yield of a chemical reaction. 108(11):4375–4378, 1998.

[27] Brett J. Pearson, Sarah R. Nichols, and Thomas Weinacht. Molecular fragmentation driven by ultrafast dynamic ionic resonances. *Journal of Chemical Physics*, 2007 (submitted).

[28] Brett J. Pearson and Thomas Weinacht. Shaped ultrafast laser pulses in the deep ultraviolet. *Optics Express*, page 4385, 2007.

[29] David Lee Phillips and Wei-Hai Fang. Density functional theory investigation of the reactions of isodihalomethanes (CH2X-X where X) Cl, Br, or I) with ethylene: Substituent effects on the carbenoid behavior of the CH2X-X species. *J. Org. Chem.*, pages 5890–5896, 2001.

[30] Herschel A. Rabitz, Michael M. Hsieh, and Carey M. Rosenthal. Quantum optimally controlled transition landscapes. *Science*, 2004.

[31] W. Radloff, P. Farmanara, V. Stert, E. Schreiber, and J.R. Huber. Ultrafast photodissociation dynamics of electronically excited CF_2I_2 molecules. *Chemical Physics Letters*, pages 173–178, 1998.

[32] Stuart A. Rice and Meishan Zhao. *Optical Control of Molecular Dynamics*. Wiley-Interscience, New York, NY, 2000.

[33] Claude Rullière. *Femtosecond Laser Pulses - Principles and Experimnets*. Springer, 2005.

[34] B. Schmidt, M. Hacker, G. Stobrawa, and T.Feurer. Lab2a virtual femtosecond laser lab. 2004.

[35] E. Skovsen, M. Machholm, T. Ejdrup, J. Thogersen, and H. Stapelfeldt. *Phys. Rev. Lett.*, 89:133004, 2002.

[36] H. Sponer and E. Teller. Electronic spectra of polyatomic molecules. *Reviews of Modern Physics*, pages 0075–0170, 1941.

[37] Benjamin J. Sussman, Dave Townsend, Misha Yu. Ivanov, and Albert Stolow. Dynamic stark control of photochemical processes. 314:278–281, 2006.

[38] Rick Trebino, Kenneth W. DeLong, David N. Fittinghoff, John N. Sweetser, Marco A. Krumbugel, Bruce A. Richman, and Daniel J. Kane.

Measuring ultrashort laser pulses in the time-frequency domain using frequency-resolved optical gating. *Rev. Sci. Instrum.*, 68(9):3277–3295, 1997.

[39] W. S. Warren, H. Rabitz, and M. Dahleh. Coherent control of quantum dynamics: the dream is alive. *Science*, pages 1581,1589, 1993.

[40] T.C. Weinacht, R. Bartels, S. Backus, P.H. Bucksbaum, B. Pearson, J.M. Geremia, H. Rabitz, H.C. Kapteyn, and M.M. Murnane. *Chem. Phys. Lett.*, 344:333, 2001.

[41] S. Witte, R. Zinkstok, W. Hogervorst, and K. Eikema. Generation of few-cycle terawatt light pulses using optical parametric chirped pulse amplification. *Optics Express*, pages 4903–4908.

[42] A. H. Zewail. *Physics Today*, 33:27, 1980.

[43] Qingguo Zhang, Una Marvet, , and Marcos Dantus. Femtosecond dynamics of photoinduced molecular detachment from halogenated alkanes. ii. asynchronous concerted elimination of I_2 from CH_2I_2. *Journal of Chemical Physics*, 1998.

[44] Qingguo Zhang, Una Marvet, and Marcos Dantus. Concerted elimination dynamics from highly excited states. *Faraday Discuss.*, 108, 1997.

[45] Xuming Zheng and David Lee Phillips. Solvation can open the photoisomerization pathway for the direct photodissociation reaction of diiodomethane: Transient resonance raman observation of the isodiiodomethane photoproduct from ultraviolet excitation of diiodomethane in the solution phase. *J. Phys. Chem. A*, pages 6880–6886, 2000.